Simulation of Fluid Dynamics and Particle Transport in Realistic Human Airways

A thesis submitted in fulfillment of the requirements for the degree of Master of Engineering

Lok-Tin Choi

B. Eng. (H2A Hons.)

School of Aerospace, Mechanical and Manufacturing Engineering

Science, Engineering and Technology Portfolio

RMIT University

March 2007

Author's Declaration

I hereby declare that this submission is my own work and to the best of my knowledge it contains no materials previously published or written by another person, nor material which to a substantial extent has been accepted for the award of any other degree or diploma at RMIT or any other educational institution, except where due acknowledgement is made in the thesis. Any contribution made to the research by others, with whom I have worked at RMIT or elsewhere, is explicitly acknowledged in the thesis.

I also declare that the intellectual content of this thesis is the product of my own work, except to the extent that assistance from others in the project's design and conception or in style, presentation and linguistic expression is acknowledged.

……

Lok-Tin Choi

Abstract

The aim of this research is to numerically study the flow characteristics and particle transport within human airways, specifically, the upper airways starting from the trachea to major bronchi. Different entering flow rates and frequencies are the major parameters varied in order to analyze the effect on particle deposition. There have been numerous flow-particle studies in human airways at the current level of knowledge, but one major contribution from this research is that realistic geometries of human airways are used to study flow-particle interaction, in which the airway models are reconstructed from computerized tomography (CT) data of real human tracheobronchial airways.

CFD techniques for this particular study are developed based on the literature review of other similar studies. The k-omega turbulence model was found to be suitable for this type of study. Evaluation and validation of the numerical approach and results were carried out by comparing with other experimental studies in terms of geometrical details, lobar flow distribution in percentage of the tracheal flow, velocity profile, and deposition efficiency. This approach was found to be appropriate. Based on the developed techniques, two aerosol delivery methods used clinically were studied. Similarly, results were compared with experimental and theoretical results for validation. It was found that breathing pattern of short inhalation and exhalation with small air volume gives better transportation of aerosol into the lung periphery and on the contrary, long inhalation with large air volume gives higher deposition rate in the first few generations of the tracheobronchial airways. Visualization techniques were also developed where deposition pattern provided easy-to-understand illustration to personnel with no engineering background. It showed that particles often concentrate along the carinal ridges at the bifurcations and inner walls leading down from carinal ridges. The study of the interaction between flow and particle described how skewed velocity profile and vortices in secondary velocity profile affected regional deposition efficiency as well as deposition pattern. The study also confirmed that right main bronchi usually capture more particles than left side as other researchers observed.

Several important findings are summarized based on this research:

- Stokes number although is a good indicator in providing regional deposition efficiency information, the local “hot-spots” still heavily rely on visualization of deposition pattern.
- Generally speaking, high flow rate and/or large particle size lead to high deposition efficiency in the first bifurcation and cartilaginous rings along the trachea.
- Bronchi in the right hand side usually capture more particles than bronchi in the left hand side.
- Particles often concentrate along the carinal ridges at the bifurcations and inner walls leading down from carinal ridges.
- In the aerosol delivery study, short inhalation and exhalation with small air volume gives lower deposition in the first six generations than long inhalation with large air volume. Therefore, if deposition into deeper locations of the lung is preferred, then slower breathing is required. On the contrary, if the treatment location is in the first few generations, then faster or moderate breathing is more ideal.
- Deposition efficiency and deposition pattern can be estimated roughly from the velocity profile along the airway.

Acknowledgements

First and foremost, I would like to express my deep gratitude to Professor Jiyuan Tu and Dr. Frank Thien, my supervisors, for their encouragement, guidance, and support throughout my graduate studies. I would like to thank my family for all their support throughout my education, with special thanks to my beloved parents Choi Oi-Yi and Chu Chun-Fa for their love, advice, and financial support.

Finally, I would also like to thank my colleagues; Huafeng Li, Dr. Zhaofeng Tian, Krishna Mohanarangam, Dr. Songlin Ding, Dr. Sherman Chi-Pok Cheung, Dr. Edsil Dilla, Kiao Inthavong, Akraphon Janon, Weng-Yew Chan and Thau Do for providing invaluable technical guidance and joyful memories throughout the course.

Table of Contents

List of Figures

List of Tables

List of Publications

1. Choi, L. T., Tu, J. Y., Li, H. F., and Thien, F. 2007. Flow and Particle Deposition Pattern in a Realistic Human Double Bifurcation Airway Model. *Inhalation Toxicology*. 19:117-131.
2. Choi, L. T., and Tu, J. Y. 2006. Flow and Particle Deposition Patterns in a Realistic Human Double Bifurcation Airway Model. Accepted and Presented for the Fifth International Conference on CFD in the Process Industries, CSIRO, Melbourne, Australia 2006.
3. Choi, L. T., Tu, J. Y., Ding, S. L., Thien, F., and Thompson, B. 2007. Numerical Study of Two Aerosol Delivery Methods in a Human Major Airway Model. <In Progress>.

Nomenclature

A	cross-sectional inlet area
C_D	drag coefficient
D	Diameter
dp	particle diameter
F_D	drag force
k	turbulence kinetic energy
L	Length
Le	eddy length scale
p	pressure
Q	Respiratory rate of inhalation
r	uniform random number
Re	Reynolds number
Re_p	particle Reynolds number
St	Stoke number
t	time
t_{cross}	particle eddy crossing time
t_p	particle relaxation time
T_L	Lagrangian integral time
u	velocity
u_i	velocity vector (same for u_j)
μ	dynamic viscosity

u^g	gas (air) velocity
u^p	particle velocity
U	mean velocity
x_i, x_j, x_k	spatial coordinate system

Greek letters

ρ	density
ω	Pseudo-vorticity
v	kinetic viscosity
τ_e	eddy lifetime
τ_i	Reynolds stress tensor

Subscripts and Superscripts

air	air phase
p	particle phase
g	gas phase
k	turbulent kinetic energy
p	discrete particle phase
t	turbulent phase

Chapter 1
Introduction

1.1 Motivations

Inhaled particle pollutants can be considered as a potential cause of respiratory diseases (Pope et al., 1995; Kreuzer et al., 2000; Balásházy et al., 2003). In addition, currently marketed inhalation therapies can only deliver 10-20% of a drug load into the lung with an effective inhalation (Clark, 1995) and Roland el al. (2004) reviewed that the extra drug load (80-90%, the rest of the drug) for certain types of drug can cause side effects to patient. Therefore, accurate prediction of local and regional pattern of inhaled particle deposition in the human airway should provide useful information to clinical researchers in assessing the pathogenic potential and possibly lead to innovation in inhalation therapies.

There have been numerous studies regarding the deposition of aerosols in the respiratory system. Aerosol drug therapy as well as deposition of toxic aerosols remain the primary areas of concern in the current study. Many works have been done to investigate the parameters that can affect the deposition of aerosols. Particle properties, breathing conditions and lung geometry are known to be the main factors influencing the deposition of aerosols. Despite using anatomical realistic airways from living humans to study aerosol deposition, different particle properties and breathing conditions have been studied extensively. Although most of these experimental and numerical works on flow in human airways were based on simplified, idealised airway models extracted from the early morphological studies completed by Weibel (1962) and Horsfield et al. (1971), there have been several works attempted to explore the flow transport numerically in realistic airways which were based on computerized tomography (CT) scanner imaging (Perzl et al. 1996; Vial et al. 2005). Thus, computational fluid dynamic (CFD) techniques combined with CT reconstructed airway model in simulating flow phenomena have been proven useful. However, there have been only few attempts to investigate both flow and particle transport together in realistic airways.

Therefore, this research was conducted to develop CFD techniques to be used to study flow structures, regional deposition efficiencies (DE) and deposition patterns and their interactions.

1.2 Thesis Aim

This study primarily focuses on adopting the CFD approach and assessing two aerosol delivery methods by comparing the airflow structures, deposition efficiencies and deposition patterns in a realistic airway. Based on this study, some recommendations in enhancing the efficiency in delivering aerosolized drugs to the intended location within the lung were drawn.

Although, particle deposition and its dynamic nature have been investigated comprehensively by experimental studies on casts of human airways and the simplified (smooth-walled) model as well as numerical studies on simplified models in different geometrical configurations, it is still unclear to what extent the results from these studies may be applied to numerical predictions based on a model of realistic human tracheobronchial airway that was replicated using CT scan data.

This is because geometrical detail may strongly affect the prediction on both the airflow and the regional particle deposition. It is thus difficult to describe the lung in terms of a simple model and hence it is unreasonable to apply the same results obtained from one particular airway model in accessing other individual airways. Therefore, this study was conducted to evaluate the potential use of CFD in realistic airways reconstructed using CT scan data in assisting practical clinical study. An airway model was reconstructed from CT scan data. The suitability and comparability of the CFD model was determined by comparing the air flow and particle deposition efficiency with other studies. Based on the developed numerical techniques, two aerosol delivery methods used clinically were studied. Some clinical recommendations were drawn.

1.3 Thesis Structure

The rationales of conducting this research, the scope and outlines of this thesis are explained in Chapter 1.

Chapter 2 provides an in-depth review of the background for this research. Some previous studies that highly related to this research are covered. There are mainly three aspects included in flow-particle studies of human airways: experimental, theoretical and numerical approaches. The methods used in these approaches, their differences, advantage and disadvantages of the methods are discussed and compared. This literature review provides the main frame of what this research will develop from.

In Chapter 3, since the main focus on this research is the realistic airway being used in the flow-particle study, the airway modeling becomes one of the important parts. Anatomical studies on lower airways are covered here. The classification of generations and the past conducting airway models that have been widely used are introduced. Based on these studies, the important issues in reconstructing the numerical model used in this research are drawn. The methods and reconstructing processes are described in the later section of this chapter.

The fundamental knowledge in numerical modeling and the chosen modeling method are listed and explained in Chapter 4. The rationale of using the chosen turbulence model and the equations being solved in this simulation are listed. Some of the common issues explored in Chapter 5 and 6 in numerical modeling are introduced.

The main body of this research starts in Chapter 5. The development and evaluation of the proposed CFD approach for flow-particle analysis covers the methods in extracting CT data, geometry generation, boundary conditions setting and numerical setup are completed. Results are verified against other similar studies. The interaction and phenomena of flow and particles in human airways are investigated based on the obtained results in terms of velocity profile, deposition efficiency and particle deposition pattern.

After the evaluation of the CFD approach, a study of comparing two aerosol delivery methods is conducted and its details of issue (i.e. velocity profile, deposition efficiency and

deposition pattern) similar to Chapter 5 are incorporated in Chapter 6. Both chapters have also included a summary of that chapter and some limitations that bounded the results in interpolating to real world scenario.

The final chapter concludes the findings and summarizes the significance of the outcomes. The deposition efficiency and deposition patterns of the flow structures of the interactions are discussed in depth. Some comparison statements with other important studies are also discussed. Final sections highlight with the potential clinical significance of this study and draw some recommendations for further study.

Chapter 2
Background and Literature Review

2.1 Background of the Study

Initial research conducted on the physics of aerosols and airflow in the human upper airway have been mainly based on experimental and theoretical studies. The velocity profile and deposition efficiency have been the focus of previous studies. The experimental approach has been used to obtain either velocity profile or deposition efficiency. Generally, experimental studies can be categorized into two major approaches, using human cadaver replicate airway models to study deposition efficiency and idealised airway models (e.g. made of smooth plastic tubes) to study velocity profile using pressure probe or dye tracing. Due to the nature of the complex setup involved in the experimental study, these two issues were often investigated separately and the interaction between fluid (airflow) and particles (aerosols) was rarely explored in experimental studies. Many of these *in vitro* experiments although provided important information, limitations were unavoidable. From a velocity profile perspective, the method of inserting the probe into a model to measure the flow can often affect the flow downstream and the measurement point. This is especially noticeable when the cross-section of the airway tube is small. Moreover, only limited sample readings are extracted due to the cost and time in the experimental setup. Thus, the amount of information provided by experimental technique is not only restricted, but the accuracy of the results can be difficult to control. The more advanced method of using laser Doppler anemometry has been applied recently in more recent research. This has resulted in improved accuracy for velocity profiles along occluded tubes without influencing the flow inside. However, a disadvantage of this method still exists. Despite the costly equipment, the complexity in preparing the equipment and the long process time in acquiring and standardizing the results remain unavoidable. Also, some crucial information, such as the boundary layer region (near wall region) of flow velocity, are extremely difficult to capture

in which this factor is one of the major influences in particle deposition on the wall of the model. In terms of measuring deposition efficiency, there are two major approaches. One of the methods involves injecting a range of polystyrene latex fluorescent particles into a hollow silicone rubber cast of human airways, and then the cast is cut into segments. Fluorescent material in the particles that deposited in the cast is extracted using ethyl acetate. The resultant solution is then filtered using a nylon membrane and the fluorescence content of the filtered solution is measured using a florescence spectrometer. The deposition fraction (i.e. efficiency) in each airway segment is calculated from this measurement. (e.g. Zhou and Cheng, 2005) Another method is to inject ferric oxide particle tagged with short-lived radioisotopic tag, then deposition activities within the cast are measured in a scintillation detector system. (e.g. Schlesinger et al., 1977) Similarly, these experimental techniques require expensive equipments and extensive time of setup. The major disadvantage in this type of approach is that the casts of the airway are replicated from a cadaver in which the shape and the angle of bifurcation of the airway are very likely to be distorted compared to living human subject after the airway is taken out from a cadaver. The lost of geometrical details can also happen during the replication process. Another limitation was also declared by Schlesinger et al. (1977) where the large number of bronchi within the cast and limitations imposed by use of a short-lived isotope tag made a complete investigation of deposition within all branches of the cast impractical. Measurements were, therefore, made within a selected sample of bronchi.

Although most of the numerical results were verified by comparing experimental results, the experimental results acquired in the past were often validated with theoretical models and other similar experimental data. The aim of the theoretical models is to provide estimation of aerosol deposition fractions (efficiencies) in the tracheobronchial airways using a simple, idealised mathematical model (such as a curved tube) which includes the selected parameters, such as, flow rate, particle size, radius of curvature of bifurcation, branching angle, length of bronchi, cross-section ratio between parent and daughter tubes, etc. It has the advantage of giving a range of initial predictions regarding deposition efficiency for certain regions in a timely manner, but they, of course, cannot be used to characterize the differential

distributions of deposition efficiencies along the airways. Based on the same reason, the theoretical results can only be used to compare with numerical and experimental data and cannot be extrapolated to realistic airway models.

Nowadays, computational fluid dynamics have been seen as an excellent technique in studying flow and particle behaviours within airways. One obvious advantage is being more economical than experimental method and it can also incorporate more complicated flow and particle phenomena in a more complex airway model than theoretical model, where simple, idealised models are often used. There have been numerous numerical studies related to flow profile, deposition efficiency and aerosol deposition pattern, where the close interactions between these three subjects have been researched. However, they have often analyzed either individually or in a simplified model (e.g. symmetrical airway model). There have been very few studies that involved all three subjects in a realistic airway model (i.e. based on CT scan) to the best of the author knowledge.

Velocity profiles within airways have been difficult to acquire completely and accurately using experimental method as mentioned previously. It is a vital indication of how particles are transported and behave in various breathing conditions. Generally, particle deposition pattern can be approximately predicted by the shape of the velocity profile at the specified location. It is therefore preferable to derive this subject numerically where computational simulations can provide three-dimensional visualization.

Regional particle deposition efficiencies are particularly of interest to clinical researchers in assessing both medication penetration efficiencies and health risk assessments of inhaled toxic particles. Regional particle deposition efficiency is a ratio of an amount of particle trapped in a specified region to the total amount entered into the model. Thus, the most likely area that can attract the particle to deposit under the given breathing condition can be found by conducting this analysis.

Deposition patterns are a recent trend in visualizing particle deposition to researchers in a more direct, informative and easy-to-read manner in which the deposition patterns can directly illustrate the “hot-spots” (the most concentrated spot of trapped particle) while this

information cannot be revealed by the analysis of deposition efficiency. Nevertheless, the analysis of deposition efficiency is a quantity indication.

Computational fluid dynamics can clearly provide insight of the behaviour of airflow and aerosols deposition which, in turn, can potentially lead to better drug delivery technique or treatment and important information for clinical practitioners in assessing the prospective health risk within the human airways by inhaled particle. From a research perspective, it can provide stable, high accuracy results in all aspects easily, which can be compared and validated with available experimental and theoretical results.

2.2 Previous Experimental Studies

The initial research into particle deposition, and velocity profile and flow distribution within human upper airways concentrated on experimental approaches. Those approaches can be categorized into two major groups, using human cadaver replicate airway models to study deposition efficiency and idealised airway models (e.g. made of smooth plastic tubes). In the view of particle deposition studies, Schlesinger et al. (1977) developed a hollow silicone rubber cast of the larynx and tracheobronchial tree which extended to bronchi of approximately 0.2 cm diameter. The cast was exposed to radioactively tagged, ferric oxide aerosols, having mass median aerodynamic diameters ranging from 2.5 to 8.1 μm, at three constant inspiratory flow rates. Their study found that bifurcation deposition generally peaked in generation 3 and high flow rate leaded to higher deposition in all generations. Similar study was also conducted by Schlesinger et al. (1982), except cyclic flow was used. Deposition efficiencies at bifurcation and length sub regions of each generation were greater under cyclic flow and these differences were greater for the smaller sized aerosol. They studied the surface density distribution on the first bifurcation and showed that higher concentration appeared at the carina ridges and the inner wall of the bifurcation under both constant and cyclic flow conditions.

Chan and Lippmann (1980) measured the particle deposition for the first six branching generations of replicate hollow casts of a human tracheobronchial tree with a mechanical

larynx and drawn some basic agreements when they compared their results with data obtained from twenty-six non-smoker human volunteers in vivo, where a liner dependence of particle deposition efficiency on the Stokes number for aerosols with aerodynamic diameters >2 μm. Cheng et al. (1999) also provided similar results as they measured deposition efficiencies in a replicate cast of human oral-tracheobronchial airways made from an adult cadaver under different flow rates. They found that 90% of particle > 20 μm would be trapped within oral cavity at the flow rate of 60 L/min. This is why particle larger than that size would not be studied in tracheobronchial airways in this research. Deposition efficiency is a unique function of the Stokes number, suggesting that impaction is the dominant deposition mechanism. Zhou and Cheng (2005) used the same method as Cheng et al. (1999) and indicated that the deposition efficiency with the larynx effect was generally larger than without it and hence the larynx affected the flow pattern of the tracheal region, causing more particles to be deposited. They also suggested that the turbulence induced by the laryngeal jet could likely persist in the first few generations of the tracheobronchial airways, resulting in higher deposition efficiencies.

Kim and Fisher (1999) established a logistic function to describe the deposition efficiency that they measured on a symmetrical double bifurcation glass tube model with dimensions similar to Generation 3 to Generation 5 (G3-G5) in Weibel's symmetrical model. Their results showed that DE (Deposition Efficiency) in each bifurcation increased with increasing Stokes number, ranging from ~ 1% at St = 0.02 to ~ 40% at St = 0.2. Their deposition pattern also showed highly localized deposition on and in the immediate vicinity of each bifurcation ridge at Stokes numbers as low as 0.02, regardless of branching patterns and flow distribution used.

From a flow profile perspective, Schroter & Sudlow (1969) observed how secondary flow formed in inspiration and expiration in a single bifurcation glass tube model using dye tracing method under either flat or parabolic profiles entering the inlet. The profile of secondary motions was dependent on the direction of flow along the tube. Double vortices were formed during inspiration in the daughter tubes. On the contrary, quadruple vortices were created during expiration in the parent tube. Depending upon the curvature of the

junction, flow separation with sluggish reversed flow could be observed in daughter tube during inspiration. Axial velocity profiles were highly asymmetric. Peak velocities swung to the inner walls. During expiration, velocity profiles developed an axial peak. Chang & El Masry (1982) measured detailed steady inspiratory velocity profiles in a scaled plastic tube model of the human tracheobronchial airways using anemometer probes, in which the model had 12 pre-drilled stations of measurement and the dimensions of their model were consistent with the lung geometry reported by Horsfield et al. (1971). Menon et al. (1984) used the same method and model from Chang and El Masry (1982) and drawn detailed velocity profiles obtained during inspiration and expiration. The results of both studies showed a high degree of asymmetry in all branches, with peak velocities near the inner wall of the bifurcation. Overall, the velocity profiles were more sensitive to airway geometry than to flow rate. However, at low oscillatory frequencies (e.g. 0.25 Hz) of inlet flow, the velocity profiles attained at peak flow rate resembled the profiles seen under steady flow conditions at the corresponding Reynolds number. As the frequency increased (e.g. 4 Hz) the velocity profiles throughout most branches tended to be flattened, the details, however, wouldn't be included here because high oscillatory frequency flow is beyond the scope of this research.

The research above demonstrates that the Stokes number is one of the important factors in determining deposition efficiency, but the researches also showed that experimental data from various studies have large variations but the same characteristic of trends for DE vs. Stokes number is still presented. Velocity profiles measured in different experiments can be comparable when correct Reynolds number, oscillatory frequency and geometrical details are met. These two issues will be good indicators in verifying the present numerical study.

2.3 Previous Theoretical Studies

Theoretical models have also been used to study regional airway deposition. They were usually designed to predict initial deposition in the tracheobronchial airways with an idealised model, such as single bifurcation model. Cai and Yu (1988) have showed that inertial deposition in an idealized, symmetrical single bifurcation is a function of the Stokes

number, bifurcation angle, and ratio of parent and daughter tube diameters. Their results were calculated based on a mathematical model they developed. They concluded that the deposition efficiency increased with the Stokes number, and was higher for the parabolic inlet flow than for the uniform inlet flow. The deposition efficiency also increased with the bifurcation angle, but decreased only slightly with the daughter-parent tube diameter ratio. Similarly, Balásházy et al. (1990) developed a theoretical model of the simultaneous action of inertial impaction and gravitational forces on a particle moving in three dimensional circular bends based on the mathematical expressions. They showed that three-dimensional model always predicted higher values than the two-dimensional model, but the difference never exceeded 25% for tube parameters which were characteristic of the human tracheobronchial tree. They also confirmed the statement of Crane and Evans (1977) that deposition efficiency was not strongly affected by secondary fluid flows in airway cross sections for the case of inhalation. An airway replica including the oral cavity, pharynx, larynx, trachea, and three generations of bronchi was developed by Cheng et al. (1999) and expressions based on the experimental data with steady inhalation were presented and shown in Chapter 6.

2.4 Previous Numerical Studies

In numerical studies, a smooth-walled (and hence simplified) airway model was mostly employed with only variation in geometry and method of dichotomy. Regular dichotomy (symmetry) airway models have been extensively studied by Comer et al. (2000a & b) and Zhang et al. (2002a & b). Irregular dichotomous airway models have also been investigated by Zhang et al. (1997) and Balásházy & Hofmann (1993). All these studies showed that the regional deposition efficiency (DE) can be expressed as a logistic function in terms of inlet Stokes (St) number for the studied bifurcation geometries.

In terms of validating CFD results, Zhang and Kleinstreuer (2002) and Comer et al. (2000 a & b) have extensively compared their numerical results with experimental results in regard to the velocity profile from Zhao & Lieber (1994) and the deposition efficiency from Kim &

Fisher (1999). They demonstrated consistent results in a steady flow condition within Stokes number ranging from 0.01-0.12. They also explained how particle trajectory was affected by airflow vortexes before and after bifurcation using G3-G5 model. Balásházy and Hofmann (1993) and Zhang et al. (1997) compared the DE with different bifurcation angles using G3-G6 symmetric model. Their results indicated that DE increased with larger bifurcation angle. Furthermore, Zhang et al. (1997) investigated DE in different Reynolds (Re) numbers and showed that DE increased with increasing Reynolds number, but became almost independent of Re when St > 0.1. The above studies used idealised model which the model geometry was hardly comparable to real human airway structure. From a realistic human airway geometry perspective, Vial et al. (2005) reconstructed the tracheobronchial airway from the CT scan data and simulated airflow. Their results were examined in terms of the lobar flow distributions with Katz and Martonen (1996) and Corieri (1994)'s results and geometrical details with Weibel (1983)'s dichotomous model. Ertbruggen et al. (2005) although used smooth-walled models, the model was based on the morphometrical date of Horsfield et al. (1971), which Horsfield and his colleagues measured all structure down to generation 6 of a resin cast of a normal human bronchial tree. They compared their numerical results from experimental results with Kim et al. (1996) in terms of regional deposition efficiency and velocity profiles with Calay et al. (2002)'s measurement. Since experiments they compared with had either respiratory or geometrical differences, some rounding errors were thus expected, but basic characteristic of flow and particle behaviours were still reflected in their results.

Zhang & Finlay (2005) proved that trachea with cartilaginous rings would enhance particle deposition in the trachea for all inhalation rates and particle sizes compared with smooth-walled trachea. The influence of larynx on the airflow and particle deposition in the trachea and its lower airways has been included in many experiment and numerical simulation through complete upper airways analysis (from oral cavity to lower generations). Zhang et al. (2005) also showed that the larynx effect caused turbulent fluctuations at medium and high inspiratory flow rates (30 and 60 L/min) due to the enhancement of flow instabilities immediately upstream of the flow dividers. Moreover, the effects of turbulent fluctuations on

micro-particle deposition were relatively important in the human upper airways. These phenomena therefore would be expected in the present study.

Asgharian and Price (2006) studied the influence of airflow distribution among bronchi on particle deposition and found that airflow rate entering each major bronchus was similar for uniform and non-uniform lung expansions and concluded that the assumption of uniform air expansion and contraction was sufficient for the predictions of regional and total deposition of particles in the lung. However, they also pointed out that accurate predictions of local and site-specific deposition of particles required more detailed models of lung ventilation that account for non-uniform lobar expansion due to the pressure variation in the pleural cavity. In this research, the assumption of uniform air expansion and contraction was taken into account, but the later issue was not considered in this study due to its complex modeling requirement.

There have been other notable researches that used CFD to study air and particle transport in the airway. However, only articles that are highly related to this research are discussed here.

Chapter 3
Modeling the Airways

3.1 Introduction

The respiratory system is divided into the upper and lower airways, the upper extending from the nasal/oral cavity to the larynx, the lower from the larynx to the respiratory bronchioli and alveoli. The lower airways are primarily focused in this study, which consist of the trachea and the main bronchus (Generation 2 and 6 in this study). Firstly, the human lower airways in anatomical terms is described in Section 3.2.1 which help to understand the features of the airways that must be noted during model reconstruction and simulation. The structure of human airways can be approximated as a network of repeatedly bifurcating tubes (Weibel, 1963). The position of a branch in relation to the stem branch can be described by Weibel generations which have been employed widely among researchers. Section 3.2.2 explains the method in more details while relating it to the current numerical model.

3.2 Background

3.2.1 Anatomical studies of the conducting airways

The trachea is a cylindrical tube with 10 to 12 cm long, about half of which is extrathoracic and half intrathoracic. According to Weibel's (1963) measurement, the diameter of the trachea is about 1.5 to 1.8 centimetres. 16 to 20 incomplete (C-shaped) rings of cartilage composed the trachea wall with fibrous and muscular tissue. The trachea divides into the two primary bronchi at the level of the fifth thoractic vertebra. There is an internal cartilaginous ridge at the point of bifurcation, called the carina.

The right bronchus is a shorter, wider tube than the left and the angle of branching from the trachea is only 20-30˚. Weibel (1963) measured the main bronchus to be 0.9 to 1.5 cm in

diameter and 4 to 6 cm in length. Consequently any foreign bodies that enter the trachea are more likely to be inhaled into the right main bronchus. This may also influence the distribution of aerosol delivery to the lungs. The details of measurement and comparison with other existing measurement of human airways are included in both Chapter 5 and 6.

3.2.2 Classifying branches in the airways

The branching pattern resembles that of a tree, with large branches giving rise to successively smaller branches in terms of length and diameter. This pattern of division varies and is probably genetically determined (Shannon and Deterding, 1997). Figure 3.1 shows how the lower airways are named and classified into generation using Weibel's generation. The numbering begins at the stem branch and continues towards the peripheral branches. The trachea has the lowest generation number, and the subsequent branch division, main bronchus has one generation higher than the parent branch, trachea. This also applies to asymmetric trees in which terminal branches are classified in a range of generations. Branches that have different diameter and length can therefore be grouped together for simple classification.

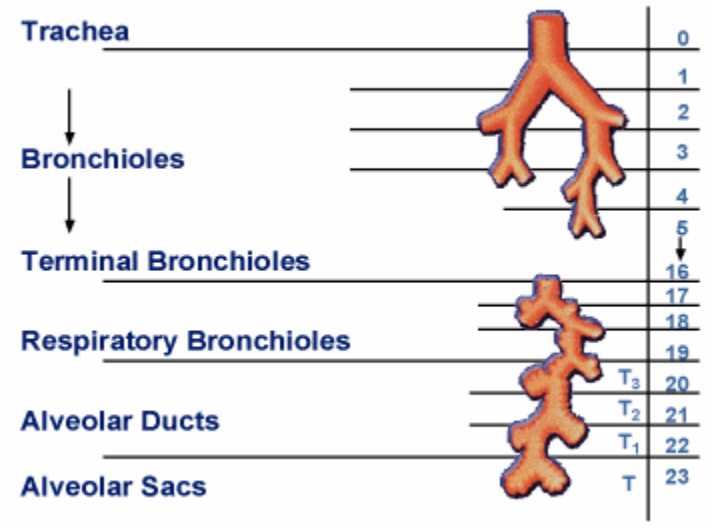

Figure 3.1 – Branching generation of the airway (Cefalu, 2003)

3.2.3 Past conducting airway models

The airways in the human lungs are a complex asymmetric branching structure. However, most of the airways models in both experimental and numerical investigations have used highly simplified models in order to reduce the computational/experimental cost and the complexity in producing the highly complex airways structure. Some of the investigations have tried to include the asymmetric features into the airway model with some idealised features. Several of the studies have used hollow cast of the human airways of a cadavers. These models are reviewed in this section.

3.2.3.1 Weibel's symmetric model A

Weibel's symmetric model A has been widely utilized by investigators of human airway study. The model was developed by Weibel in 1963 based on the measurement on the major conducting airway branches from a plastic cast of a pair of human lungs. Weibel analyzed and found the correlation on diameter and length of branches as well as distribution correlations of diameter and length in every generation. Although only first four generations and 10% of the rest of the generation were measured precisely, due to the difficulty in measuring the small bronchioles, regular dichotomy and a mean branch length to diameter ratio were assumed and from these measured data, Weibel's symmetric model A with regular dichotomy and fixed length to diameter ratio was developed.

The symmetric model has been used to investigate flow distribution and particle deposition in both experiment and numerical simulations. Some of the articles used this model were showed in Chapter 2 – Literature Review. Zhang et al. (2005) used this model extensively in their studies of air-particle flow. The model reconstructed by them is shown in Figure 3.2 .

There are some disadvantages in using this model. For example, the results obtained in this model can hardly extrapolate into real human airway structure, especially this model excluded the asymmetric factor of real human airways. On the contrary, it can definitely reduce the time and cost in reconstructing the model both numerically and experimentally because of its simple structure. In addition, it makes more accessible to verify results among different investigators who used the same model.

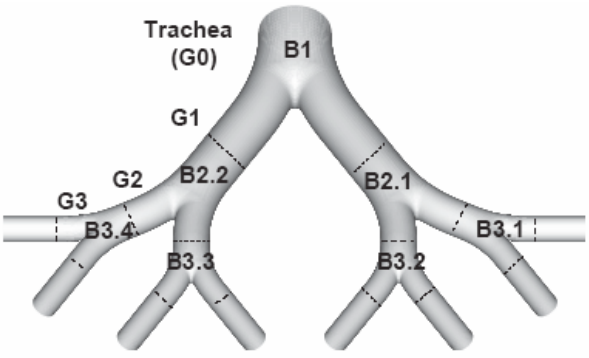

Figure 3.2 – Symmetric airway model reconstructed by Zhang et al. (2005) based on Weibel symmetric model A's measurement

3.2.3.2 Horsfield's Delta model

Horsfield and Cumming (1968) performed detailed measurements on a resin cast of the human lungs. 8,298 branches were measured from the trachea down to lobular branches. Based on their previous work, Horsfield et al. (1971) derived an asymmetric conducting airway model. The asymmetric model was based on the concept of regular asymmetry at different levels in the airway tree. Similar to Weibel (1963)'s work, they measured not only the diameter and length of branches, but they also obtained the flow distribution in terms of the percentage of tracheal flow, which proved to be very useful reference in the later stage in comparison with other measurements on human airways. Erthruggen et al. (2005) employed Horsfield's Delta model in reconstructing their computational model as well as implementing the flow distributions measured by Horsfield et al. (1971) in their numerical simulation. The numerical model reconstructed by Erthruggen et al. (2005) is shown in Figure 3.3 .

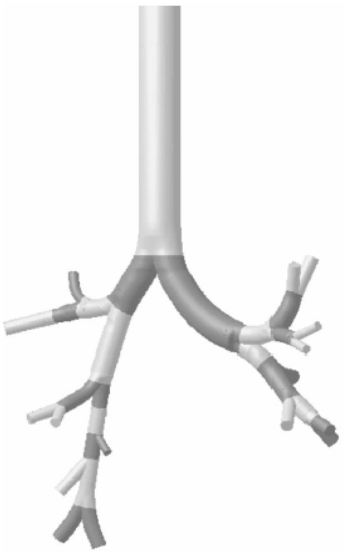

Figure 3.3 - Airway model reconstructed by Erthruggen et al. (2005) based on Horsfield et al. (1971)'s measurement

Although, Horsfield's Delta model was based on the measurement of a resin cast of normal human bronchial airways and most of the critical dimensions, such as dimension, length, branching angle and flow distribution in percentage of the tracheal flow were provided in their study, some information were not included, such as angles measured in three-dimensional space including, gravity angle, coronal angle and sagittal angle as shown in Figure 3.4 .

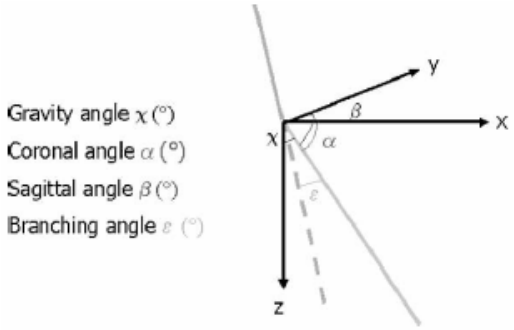

Figure 3.4 – Spatial Orientation of airway branches (extracted from Vial et al., 2005)

As Figure 3.3 shown, Erthruggen et al. (2005) assumed daughter branches were 90 degrees out-of-plane to their parent branches. In fact, daughter branches in real human airways were, of course, in various twisting angle to their parent branches. Therefore, more realistic modeling methods were still implemented in air-particle study in human airways in other studies, which will be described in the next section.

3.2.3.3 Human airway cast

The last two methods were based on the measurement of a human airway casts from cadavers with their own developed simplification method in reconstructing the model. However, there have been numerous experiments carried out using airway cast from cadaver to study air-particle phenomena. As mentioned in literature review in Chapter 2, a portion of experimental studies showed that airway cast often made of silicone rubber because of its user-friendliness in reconstruction. It can be easily cut into specified segments for regional particle deposition measurement and hence, results can be compared with other studies. Using conductive material can also eliminate particle deposition in the replica due to the electrostatic effect. In Figure 3.5 , the replica consists of an oral cavity, oropharynx, larynx, trachea, and the tracheobronchial airways to the 4th bifurcation. It was reconstructed by Su and Cheng (2006) using silicone rubber and the model was molded from a cadaver. In the deposition experiment, the inside wall of the cast was coated with silicon oil to simulate the mucus inside the wall of human airways.

Figure 3.5 - Airway model reconstructed by Su and Cheng (2006) using silicone rubber molded from a cadaver

3.3 Developing a computational airway model

3.3.1 Introduction

Based on the previous literature reviews, there is a need to study air-particle phenomena in realistical reconstructed airways to verify the simplified studies both numerically and experimentally. In order to achieve the accurate reconstruction of airways, Compute Tomography (CT) scans of patient were used. The methods of extracting useable data from CT scan in reconstructing airway model for CFD use were different in both studies (i.e. Chapter 5 and 6). In Chapter 5, an algorithm was developed to read the outlines of every slice of CT scan (in X-Y plane) respected to its vertical position (Z location of the slice) in a 3-D space in which was stored as IGES file (Initial Graphics Exchange Specification). The principles of how the algorithm work is similar to Aykac et al. (2003) work. This method was time consuming and contained lots of manual works in the reconstructing process. During the process, a portion of details of airways were lost. An airway reconstructing software based on the given CT scan was later found and it is developed by VIDA diagnostics (Technology Innovation Center, Iowa City of U.S.A.). This software worked in similar manner as described in Chapter 5, but it can automatically adjust (smoothing the surface of model) and

distinguish the generations in the airways. This has dramatically reduced the time in reconstruction. However, some manual adjustments for CFD use were still required since the software was not designed to give computer model that can be read into CFD software to run simulation directly. The following section will describe some of the manual work that has been done in GAMBIT (a preprocessor software in geometry and mesh generation).

3.3.2 Reconstruct airway model using GAMBIT

There are two boundary conditions that VIDA diagnostics cannot provide in their model, inlet and outlet, holes for fluid to go in and out. The model provided by VIDA was a completely closed model. Therefore, inlet and outlets have to be created along the trachea and the lowest generations in the given airway model by "cut" thought the corresponding airways (trachea for inlet and lowest generations for outlets) using GAMBIT, where the sectioned planes were perpendicular to the axis of the corresponding airways. The details of the CFD boundary conditions for these inlet/outlet were discussed in sections 5 and 6. The models provided by VIDA and preprocessed by GAMBIT (i.e. ready to use in FLUENT for simulation) are shown in the left and right side of Figure 3.6 respectively. As shown in Figure 3.6 , extended tubes were attached at the lowest generations for numerical purpose (detailed discussion included in Chapter 5 and 6). At the top of the trachea was also modified and an inlet was attached. Some modifications have also been done, such as correcting overlapping surfaces in VIDA's model, smoothing some of the unreasonable sharp curves in the airway if meshing difficulty were met. Finally, bifurcation regions were segmented in the model in order to obtain regional particle deposition measurement.

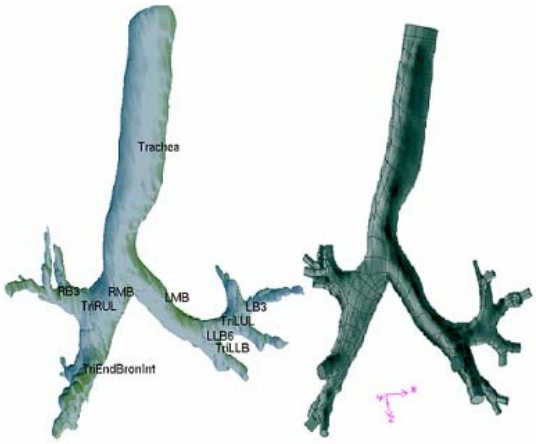

Figure 3.6 – Before and after prepossessing using GAMBIT in airway reconstruction

3.3.3 Mesh Methods

Since the airway model studied here was a complex geometry, unstructured tetrahedral mesh was chosen to discretize the computational domain of the model. To obtain the most efficient mesh size without compromising too much in result's accuracy, a mesh independent test was carried out in the first airway model discussed in Chapter 5 – Evaluation of CFD Approach for Flow-Particle Analysis. Axial velocity profile was chosen to be the parameter in determining the final outcome. Four different grid size models (approximately 50,000, 450,000, 1,600,000, and 2,100,000 elements) were tested and compared as shown in Figure 3.7 . The results started to become more independent of the grid size at 450,000 elements. In order to make a compromise between the result's accuracy and computational cost, a model with 450,000 elements was utilized in which the individual grid size was approximately 1 mm (unit in GAMBIT's term). The views of finite volume mesh of the model were illustrated in Figure 5.1 .

In the second study of two delivery methods of aerosols in Chapter 6, the airway model contained more generations than the model in the first study. Therefore, finer meshes were to be expected in lower generations because of the narrower regions. Only the first three generations (as the first studied airway model, from generation zero (trachea) to generation 2)

were discretized with grid size 1 mm. The mesh size was gradually decreased when approaching smaller bronchi as shown in Figure 6.2 .

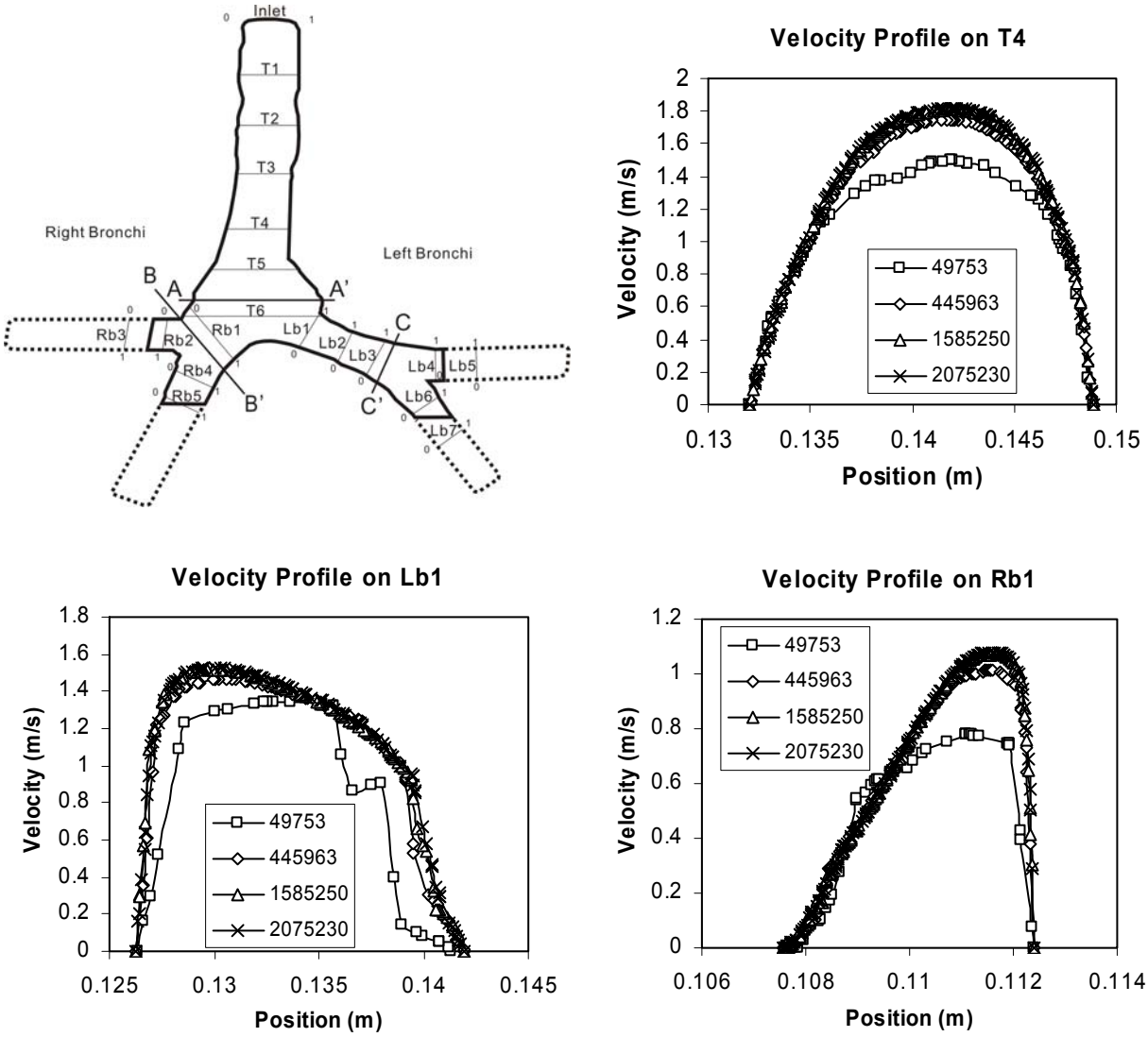

Figure 3.7 – Velocity profiles in mesh independence test. Station locations from the model of the first study in chapter 5.

Chapter 4
Numerical Simulation Approach

4.1 Introduction

This chapter provides the numerical model used with the corresponding rationale. An overview on the mathematical equations solved in the numerical process has also been explained. However, the details of setting the boundary conditions and discrete phase modelling method for the solid phase (particles) are not discussed here, because different settings have been performed in both studies (Chapter 5 and 6). The major difference between the cases in Chapters 5 and 6 is that one is a steady-state simulation because of the assumption of constant flow rate; the other is in unsteady-state because of the transient flow of cyclic flow simulation. Therefore, the first term in Equation 4.2, 4.3 and 4.4 are cancelled in the study of steady-state simulation in Chapter 5.

4.2 Modeling Gas-Particle Flow

4.2.1 Turbulence Models

According to Wilcox (1998), the low Reynolds number (LRN) k-ω model should be used in capturing the air flow structures in the laminar to turbulent flow regimes for internal flow (Zhang and Finlay, 2005). Zhang and Kleinstreuer (2003) and Varghese and Frankel (2003) demonstrated that it was appropriate for such conditions. Bardina et al. (1997) also proved that LRN k-ω model predicted the behaviour of attached boundary layers in adverse pressure gradients more accurately than k-ε model.

4.2.2 Gas-Particle Transport Equations

For incompressible flow, the fluid transport equations can be written as:

Continuity equation

$$\frac{\partial \overline{u}_i}{\partial x_i} = 0 \tag{4.1}$$

Momentum equation

$$\frac{\partial \overline{u}_i}{\partial t} + \overline{u}_j \frac{\partial \overline{u}_i}{\partial x_j} = -\frac{1}{\rho}\frac{\partial p}{\partial x_i} + \frac{\partial}{\partial x_j}\left[\left(\nu + \nu_T\right)\left(\frac{\partial \overline{u}_i}{\partial x_j} + \frac{\partial \overline{u}_j}{\partial x_i} \right) \right] \tag{4.2}$$

Turbulence kinetic energy (k) equation

$$\frac{\partial k}{\partial t} + \overline{u}_j \frac{\partial k}{\partial x_j} = \tau_{ij} \frac{\partial \overline{u}_i}{\partial x_j} - \beta^* k\omega + \frac{\partial}{\partial x_j}\left[\left(\nu + \sigma_k \nu_T\right)\frac{\partial k}{\partial x_j} \right] \tag{4.3}$$

Pseudo-vorticity (ω) equation

$$\frac{\partial \omega}{\partial t} + \overline{u}_j \frac{\partial \omega}{\partial x_j} = \alpha \frac{\omega}{k} \tau_{ij} \frac{\partial \overline{u}_i}{\partial x_j} - \beta\omega^2 + \frac{\partial}{\partial x_j}\left[\left(\nu + \sigma_\omega \nu_T\right)\frac{\partial \omega}{\partial x_j} \right] \tag{4.4}$$

For convenience, summation notation is used with $i, j = 1,2,3$ where u_1, u_2, u_3 and x_1, x_2, x_3 are the x, y, z components of the velocity vector and the spatial coordinate respectively. The symbols in the above equations, $t, \rho, p, \nu, \nu_T, \tau_{ij}, k$ and ω, are time, density, pressure, kinetic molecular viscosity, turbulent viscosity, Reynolds stress tensor, turbulence kinetic energy, and dissipation per unit turbulence kinetic energy, respectively. ν_T is given as $\nu_T = C_\mu f_\mu k/\omega$, and the function f_μ is defined as $f_\mu = exp[-3.4/(1+R_T/50)^2]$ with $R_T = k/(\mu\omega)$ and μ being the dynamic molecular viscosity ($\mu = \rho\nu$). $C_\mu, \alpha, \beta, \beta^*, \sigma_k$, and σ_ω are turbulence constant, i.e. (Wilcox, 1998): $C_\mu = 0.09$, $\alpha = 0.555$, $\beta = 0.8333$, $\beta^* = 1$ and $\sigma_k = \sigma_\omega = 0.5$.

For a low volume fraction (less than 10-12% of the gas phase, FLUENT Inc., 2003) of dispersed second phase (particle), an Eulerian-Lagrangian approach has been used. Trajectories of individual particles can be tracked by integrating the force balance equations

on the particle. The equation (4.5) did not include other possible forces (gravity, Brownian force and Saffman's life force) that a particle may experience during a real world experiment and hence, a simple eigensystem analysis is applicable in this study. Harrington et al. (2006) indicated that different orientations of gravitational force had a significant effect on the overall particle deposition predicted, which varied by a factor of approximately 3 between the orientations with highest and lowest deposition in a single bifurcation airway model with particle size range of 1 to 5 μm. To provide more assessable results in other types of research, such as particle deposition in micro-gravity environment or drug particle deposition in lay down positions, gravitational force is being neglected in this study. Secondly, the Brownian force can be neglected, since these effects should only be included for sub-micron particles only (Ounis et al., 1991). Thirdly, the particulate material considered is far denser than air, causing terms that depend on the density ratio, such as the pressure force, buoyancy force, virtual mass effect and Basset force to be very small (Crowe et al., 1998). Finally, the Saffman's lift force cannot be included due to relatively large particles and low-level fluid shear fields. Moreover, it is recommended to include this force only for sub-micron particles (Li and Ahmadi, 1992). Zhang et al. (2002b) confirmed these assumptions in validating the particle deposition results in a triple bifurcation lung airway model with experimental results. Correspondingly, the simplified particle trajectory equation (i.e., Equation (4.5)) was shown to produce reasonable particle deposition predictions compared with measurements from Kim and Fisher (1999) and Schlesinger et al. (1982).

Particle trajectory equation

$$\frac{du_i^p}{dt} = F_D\left(u_i^g - u_i^p\right) \tag{4.5}$$

The drag force per unit particle mass is $F_D\left(u_i^g - u_i^p\right)$ and F_D is given by

$$F_D = \frac{18\rho}{\rho_p d_p^2}\frac{C_D \,\mathrm{Re}_p}{24} \tag{4.6}$$

Re_p is the particle Reynolds number, which is defined as

$$\mathrm{Re}_p \equiv \frac{\rho d_p \left| u^p - u^g \right|}{\mu} \tag{4.7}$$

where u^g, u^p, μ, ρ, ρ_p and d_p are gas (air) velocity, particle velocity, molecular viscosity of the fluid, fluid density, particle density and particle diameter, respectively.

The drag coefficient, C_D, is evaluated from an experimental-fitted expression

$$C_D = a_1 + \frac{a_2}{\mathrm{Re}_p} + \frac{a_3}{\mathrm{Re}_p} \tag{4.8}$$

where a_1, a_2, and a_3 are constants that apply for smooth spherical particles over several ranges of Re_p given by Morsi and Alexander (1972). One way coupling is assumed between the air and particle flow fields due to small particle size. Also, the interaction between particles is neglected to reduce computational cost.

By using stochastic tracking method as part of the Eulerian-Lagrangian approach, FLUENT predicts the turbulent dispersion of particles by integrating the trajectory equations for individual particles, using the instantaneous fluid velocity, $u_i^g + u_i'(t)$ along the particle path during the integration process. With this method, discrete random walk or "eddy lifetime" model, is applied where the fluctuating velocity components, u_i' that prevail during the lifetime of the turbulent eddy are sampled by assuming that they obey a Gaussian probability distribution, so that

$$u_i' = \xi \sqrt{\overline{u_i'^2}} \tag{4.9}$$

where ξ is a normally distributed random number, and the remaining right-hand side is the local root mean square (RMS) velocity fluctuations that can be obtained (assuming isotropy) by

$$\sqrt{\overline{u_i'^2}} = \sqrt{2k/3}\,. \tag{4.10}$$

The interaction time between the particles and eddies is the smaller of the eddy lifetime, τ_e and the particle eddy crossing time, t_{cross}. The characteristic lifetime of the eddy is defined as

$$\tau_e = -T_L \log(r) \tag{4.11}$$

where T_L is the fluid Lagrangian integral time, $T_L \approx 0.15/\omega$. The variable r is a uniform random number between 0 and 1. The particle eddy crossing time is given by

$$t_{cross} = -t_p \ln\left[1 - \left(\frac{Le}{t_p \left|u_i^g - u_i^p\right|}\right)\right] \tag{4.12}$$

where t_p is the particle relaxation time ($= \rho_s d_p^2 / 18\rho_g \nu_g$), Le is the eddy length scale, and $\left|u_i^g - u_i^p\right|$ is the magnitude of the relative velocity. The particle interacts with the fluid eddy over the interaction time. When the eddy lifetime is reached, a new value of the instantaneous velocity is obtained by applying a new value of ξ in Equation (4.9).

Chapter 5
Evaluation of CFD Approach for Flow-Particle Analysis

5.1 Introduction

In order to evaluate the potential use of CFD in conducting flow-particle analysis in human airway models, numerical setup and reconstruction techniques of airway model have to be tested by validating the results with other data from similar numerical and experimental studies. The process in carrying out this investigation is described in this chapter. The methods in obtaining the CT scans data, reconstruction techniques and processes in reconstructing the final airway model are discussed, and then the testing conditions and how it was chosen are shown. Results are validated in terms of deposition efficiency and axial velocity profile. Finally, the correlation between airflow and particle deposition are found and explained.

5.2 Methods

5.2.1 CT Scanning

Airway geometry was obtained through a computed tomography (CT) scan of the airways of a healthy 25 year old, non-smoking Asian male (170 cm height, 75 kg mass) for the first three generations (from trachea – G0 to lobar bronchi – G2, hence Generation 0 to Generation 2). CT scan was performed using a CTI Whole Body Scanner (General Electric). The single-matrix scanner was used in helical mode with 1-mm collimation, a 40-cm field of view (FOV), 120 kV peak and 200 mA. At baseline, 2 cm axial length of lung caudad to the inferior pulmonary ligament was scanned during a single breath-hold, which yielded 112 contiguous images (slices) of 1-mm thickness with voxel size 0.25*0.25*1 mm.

5.2.2 Geometry Generation

The CT data was fed into an airway tree segmentation algorithm that can automatically identify the airway lumen in the CT image. Then the algorithm provided the outlines of every slice (in X-Y plane) respected to its vertical position (Z location of the slice) in a 3-D space in which was stored as IGES file (Initial Graphics Exchange Specification). The principles of how the algorithm work is similar to Aykac et al. (2003) work. Based on the IGES file, GAMBIT was used to create face, volume, mesh and modification using the outlines given by the algorithm. Finally, a mesh file was produced by GAMBIT in which was read into FLUENT. With the given CT scan data of human tracheobronchial airways consisting of the trachea and the main bronchi, a model was reconstructed as depicted in Figure 5.1 (b). Figure 5.1 (a) illustrated how the measurement of the dimension of the airways was conducted and how the bifurcation and generation were segmented in the airways. The approximate geometric measurements of the model are provided in Table 5.1 . The measurement was completed by using GAMBIT. Small modifications were made to the model to round sharp curves and to extended bronchus (as shown in Figure 5.1 (a)) in order to avoid back-flow phenomena that may affect the convergence process. (FLUENT Inc., 2003)

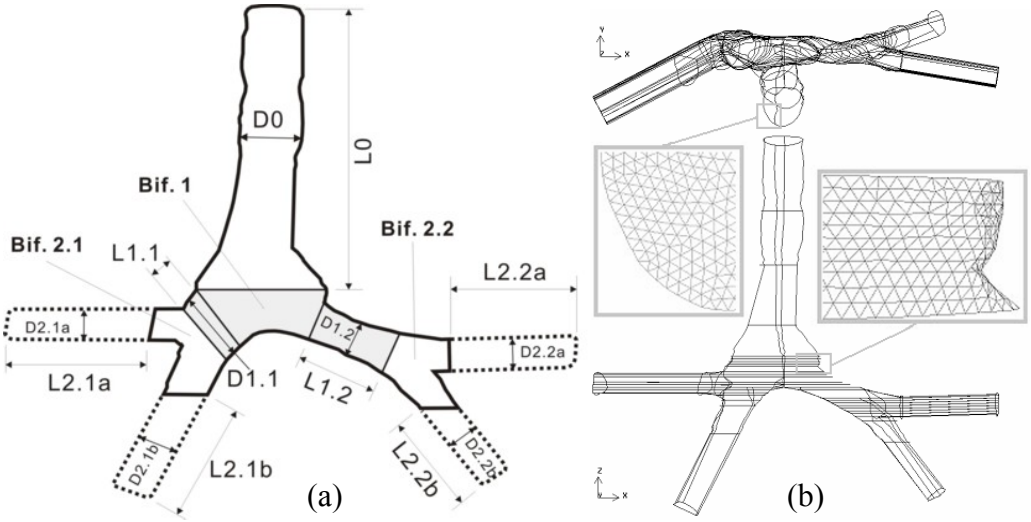

Figure 5.1 – Realistic double bifurcation airway geometry (a) model segmentation (bifurcations and generations, the shaded region indicates the first bifurcation and the dashed line indicates the extended tubes for CFD purpose) (b) finite volume mesh (the top view of the airway model indicates that all the tubes are not in plane)

Table 5.1 – Morphometry of the tracheobronchial tree model

	Generation								
	G0	**(Trachea)**			**G1**			**G2**	
		CFD			CFD			CFD	
Diameter (cm)	D0	1.54	(WM) 1.9	D1.1	1.65	(WM) 1.25	D2.1a	0.99	(WM) 0.91
							D2.1b	1.1	
				D1.2	1.02		D2.2a	0.83	
							D2.2b	0.84	
Length (cm)	L0	9.26	(WM) 1.1	L1.1	0.73	(WM) 2.9	L2.1a	4.55	Not Applicable
							L2.1b	3.11	
				L1.2	1.79		L2.2a	3.75	
							L2.2b	2.57	
Branching Angle (°)	Not Applicable			A1.1	52	(VS) 12-78	A2.1a	38	(VS) 12-78
							A2.1b	24	
				A1.2	67		A2.2a	25	
							A2.2b	28	

Note. (CFD), CFD model Measurement; (WM), Weibel (1963)'s measurement on a cadaver's airway (mean value); (VS), Sauret el al. (2002)'s measurement on a health male volunteer's airway using CT images. Data are the range value for all generations.

5.2.3 Simulation Conditions and Boundary Conditions

Inlet flow rates were simulated at 15, 30 and 60 litres per minute and the associated particle size were tested in the range of 1 to 20 micrometers in diameter for three practical reasons: firstly, most of the experimental and numerical data available have been obtained under these particular inlet flow rates; secondly, the flow rates are typical of what a human would experience during different exercise conditions; thirdly, the chosen particle size range is typical of those particles from inhalers that can reach the first few generations of airways (consisting of the trachea and the main bronchi). The parameters of the inlet flow and associated particle characteristics are summarized in Table 5.2 .

Table 5.2 – Representative respiration data and particle parameters

Physical state	Resting	Light activity	Moderate exercise
Respiratory rate of inhalation (Q, L/min)	15	30	60
[a]Mean Reynolds number at inlet	1447	2894	5789
Particle diameter (dp, μm)	1 − 20		
Particle density (ρ_p, kg/m3)	1550		
[b]Mean Stokes number at inlet	0.00042−0.17	0.0008−0.33	0.002−0.66

Note. U, D, ρ_{air}, μ, ρ_p and d_p are mean velocity evaluated as Q/A (A is the cross-sectional inlet area), inlet diameter, air density, air dynamic viscosity, particle density and particle diameter, respectively.

[a] Reynolds number, $\mathrm{Re} = UD\rho_{air} / \mu$

[b] Stokes number, $St = \rho_p d_p^2 U / (18\mu D)$

Velocity inlet was used at the trachea inlet and set as constant velocity. The airway wall was set as a trap in particle boundary condition based on the assumption that the wall of the airway is usually wet, and so once a particle hits the wall it would be trapped. Outflow (refer to FLUENT Inc., 2003) was chosen for all outlets. The overall flow distribution in present simulation was assumed to be uniformly distributed to all outlets and hence all outlets had the same flow rates.

A constant profile of particles was injected at the inlet of the model. The rationale for using constant entrance profile rather than parabolic profile in which seems to be closer to reality, is that the entrance profile is in fact unknown to what degree and skewed level of the profile should be after larynx effect. Zhang et al. (2005) already demonstrated that different flow rates and particle sizes would affect the particle deposition in the trachea after glottis and hence the particle profile would be distorted somehow due to distorted flow profiles, secondary flows and turbulent dispersion. For a simpler approach, a constant entrance profile of particle was chosen.

5.2.4 Numerical Methods

The numerical solutions of the fluid flow equations were solved using a user-enhanced, commercial finite volume based program, FLUENT 6.1.22 (FLUENT Inc., 2003). The segregated method with implicit formulation was chosen to solve the steady-state governing equations by considering incompressible flows in the present simulation (The unsteady terms at the front of the equations listed in Chapter 4 were not included in steady state). The advantage of the fully implicit scheme is that it is unconditionally stable with respect to time step size. The SIMPLEC algorithm with under-relaxation was selected for the pressure-velocity coupling.

The pressure interpolation scheme was set to second order. The convective terms of the transport equations were all discretized using second-order-upwind scheme in order to obtain sufficiently accurate solutions. For stable and accurate iterative process, the relaxation factors for momentum and pressure were set to 0.3 and 0.1 respectively. In addition, the residual values of the governing equations and the transport equations (k-ω) were all set to converge at 10^{-4}.

The particle trajectory equations were solved by FLUENT 6.1.22 using stochastic tracking model and random-Eddy-lifetime (random walk) model while the effect of instantaneous turbulent velocity fluctuations on the particle trajectories for each time step was calculated after a converged flow fields was achieved. The drag parameter of the injected particles was specified to be a smooth and spherical object.

The final number of particles and the particle flow rate were determined by increasing the number of particles inhaled (1μm was used) and decreasing the particle flow rate (kg/s) until the deposition efficiency became statistically independent of the total number of particles. The DE is defined as the ratio of the number of particles deposited in a given region to the total number entering the region. The final number of particles was determined to be approximately 180,000 during one constant inhalation, in order to achieve statistical independence of particle deposition prediction. Due to the low volume fraction (10-12%) of particles over fluid, one-way coupling between these two phases was assumed; i.e., the flow

influences the paths of the particles, but the particles do not affect the flow (Crowe et al., 1996).

A 3-D model of the tracheobronchial airway was obtained from the CT scan and imported into the GAMBIT pre-processor software package. This particular model was meshed with 0.45 million tetrahedral cells. Determination of this grid/mesh size was explained in section 3.3. All calculations were performed on a Dell P4 3-GHz PC workstation with 1 GB of RAM. The CPU time was approximately 4 hours for every case.

5.3 Model Validation

The DE of aerosol particle in double bifurcation airway model for different flow rates and particle sizes (i.e. Stokes number) has been validated with various experimental data sets (cf. Kim & Fisher, 1999; Schlesinger et al., 1982). Kim & Fisher (1999) suggested modified logistic functions to describe DE vs. Stokes number for the first two bifurcations, which were based on the trend lines fitted on experimental data using double-bifurcating symmetrical glass tube models with steady inhalation. However, the equation was bounded in range of St 0.01 to 0.2 due to the setting of the experiment. Schlesinger et al. (1982) measured the DE on the replicate hollow casts from a solid cast of a human tracheobronchial tree for the first five branching generations. Similarly, the DE was plotted against the Stokes number for different bifurcations under constant flow rates. Figure 5.2 shows the experimental data and CFD predicted deposition efficiencies for the first two bifurcations in range of St 0.01 to 0.12. When comparing the experimental results between a replicate human cast model and a symmetrical glass tube model, there is small differences in DE when the Stokes number is less than 0.1. Similarly, when comparing DE between CFD prediction and experimental data, the differences are approximately within 5% in DE value.

Due to the difficulty in precisely controlling the experimental conditions, such as flow rate and aerosol size, the Reynolds number and Stokes number fluctuated in a measurable range. In addition, the small differences between the experimental measurements and computational predictions can be caused by discrepancies in model geometries (e.g. branching angle of

bifurcation, bronchial length, etc.) and the method of deposition measurements. In addition, Zhang and Finlay (2005) proved that cartilaginous rings increase DE significantly in the trachea and conjectured that cartilaginous rings may be a critical element in influencing the prediction of particle deposition. Since the model was constructed based on a realistic airway, the model is unique in terms of geometrical details. Therefore, it is not practical to divide the bifurcation zones and generations based on other results that were mentioned previously. However, the general configuration in dividing the bifurcation zones were cautiously compared with the experimental setup by Kim & Fisher (1999) and Schlesinger et al. (1982) in order to achieve comparable results. Therefore, when neglecting the experimental uncertainties and differences in geometry, the characteristics of the CFD results correspond to the experimental data reasonably well.

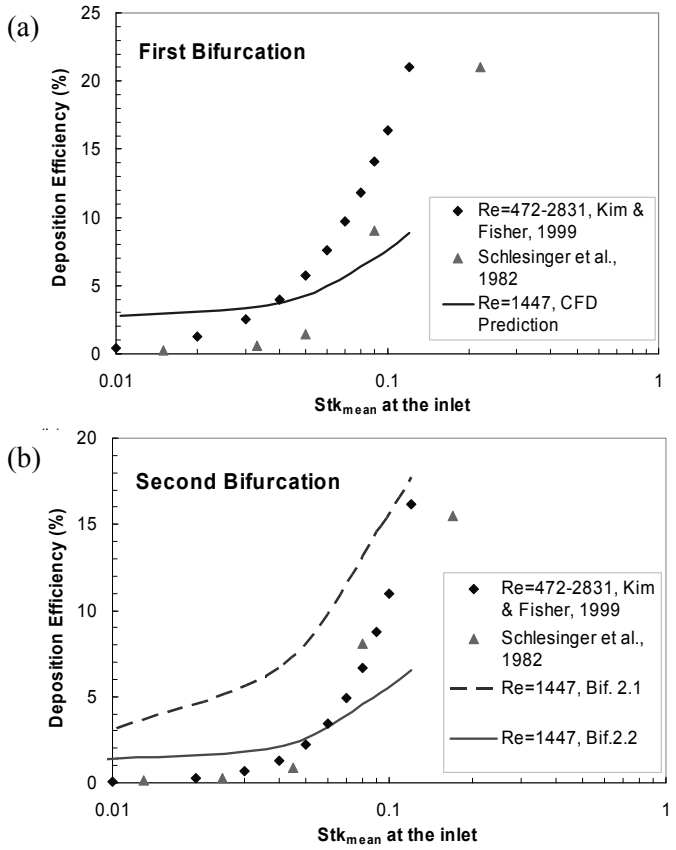

Figure 5.2 – Comparison of the predicted and experimental particle deposition efficiency (DE) in double bifurcation models under steady inhalation (a) DE at the first bifurcation; and (b) DE at the second bifurcation.

In summary, the present CFD model is proven by the reasonable agreements between experimental data and other CFD predictions. The results show that the current CFD model setting is sufficient to provide tolerable accurate information in terms of fluid-particle dynamics and particle deposition in a realistic double bifurcation lung airway model.

5.4 Results and Discussion

5.4.1 Axial Velocity and Secondary Velocity Profiles

In order to investigate the development of particle deposition within airways, the normalized axial and secondary velocity profiles of air flow are drawn and two inspiratory conditions (resting and moderate exercise) were compared. Figure 5.3 shows two sets of axial velocity profiles in the trachea at two flow rates (15 and 60 l/min). The flow rate used here corresponds to the flow rate in the trachea. In Figure 5.3 (c), the positions of stations for axial velocity profiles are marked with the thinner line with letter T, Lb or Rb next to it and the abscissa (0 and 1) shows how the lines are placed in the profiles. Similarly, secondary velocity profiles (in Figure 5.4) are marked with a thicker line with A-A', B-B' or C-C' marks which specify the position of sections. The velocity profiles were validated with Chang and El Masry's (1982) experimental data (plotted as square dots), in which they measured steady inspiratory velocity profile using a scaled human tracheobronchial airways model, which the model configurations were very close to the CFD model used here. The numerical results generally have good agreement with experimental results in terms of characteristic features. The small differences in some of the stations are to be expected since the experimental model was made of smooth plastic tubes. Also, the flow rate used in experiment and numerical simulation were different. The Reynolds numbers obtained in trachea were 2123 and 8846 in Chang and El Masry's (1982) experiment compared to1447 and 5789 in this numerical study.

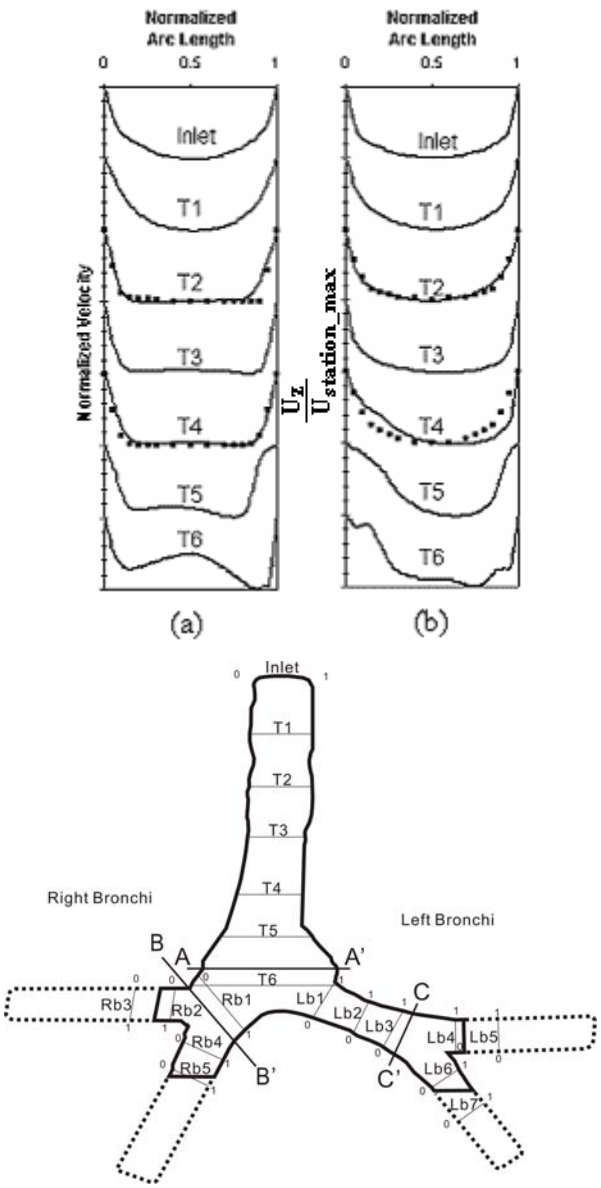

(c)

Figure 5.3 – Normalized velocity profile at trachea for an inspiratory flow rate at (a) 15 l/min and (b) 60 l/min, plotted as a function of the normalized arc length. The experimental data of Chang & El Masry (1982) are plotted as (■) for the corresponding stations. Abscissa 0 and 1 correspond to the marks, 0 and 1 in (c). (c) View of station position (The letter T represents Trachea; Rb and Lb represent the Right and Left side of Bronchus respectively. The thicker line with A-A', B-B' and C-C' indicate the position of section that is taken to visualize the secondary flow in Figure 5.4). Axial velocity scale is 0 to 1 for each profile. Normalized Velocity = Velocity / Max Local Velocity (at that profile).

Figure 5.3 (a) and (b) show that both entering profiles were of a parabolic shape, although they were beginning to develop into a different profile shape, due to the different flow rate. Figure 5.3 (a) shows that the profiles from station T2 were flatter than the profiles in Figure 5.3 (b). Also, the profiles started to develop into a bi-peak structure from station T5 to T6. Comparatively, the profiles in Figure 5.3 (b) were parabolic in shape and these shapes almost stayed the same until the flow met the first bifurcation. The reason that the higher flow rate (60 l/min) had a parabolic shape was due to higher viscous effects, which were gradually propagated toward the centre of the trachea. In other words, the less viscous effect in the lower flow rate (15 l/min) caused a flatter shape in the centre of the trachea. In addition, both velocity profiles at T5 had a low velocity zone near either one or both ends but both profiles at T6 show that the fluid recovered its inertia force. This phenomenon indicates that there were flow separations between T5 and T6 near the outer wall due to a sudden change in diameter. However, the higher velocity profiles at T4 to T6 also show that, due to greater inertial force, the flow separation seemed to be more sensitive to change in diameter. T4 already shows a drop in velocity near right side (abscissa 0) of the wall and continued this low velocity till the fluid met the first bifurcation. Therefore, the velocity profile in the lower flow rate at station T6 was more moderate compared to the higher flow rate, which had peak flow concentrated in the middle of the airway.

Similarly, the secondary velocity profile (sectional view of airflow) in Figure 5.4 (section A-A") also reflects the characteristic of the peak structure (high velocity zone in lightest colour) in both flow rates. The lower flow rate had the high velocity zone distributed more evenly over the left and right bronchus, as indicated by velocity contour graph. On the contrary, the higher flow rate had the high velocity zone concentrated in the middle of the trachea. The secondary velocity vector graph is also a good indicator of showing how particles are distributed within airways. It shows that the direction of the flow in lower flow rate had a "more complete shape" and larger vortex than higher flow rate whereas the vortex in left hand side of Figure 5.4 (b) (right bronchus) was weak in velocity magnitude and displayed turbulence.

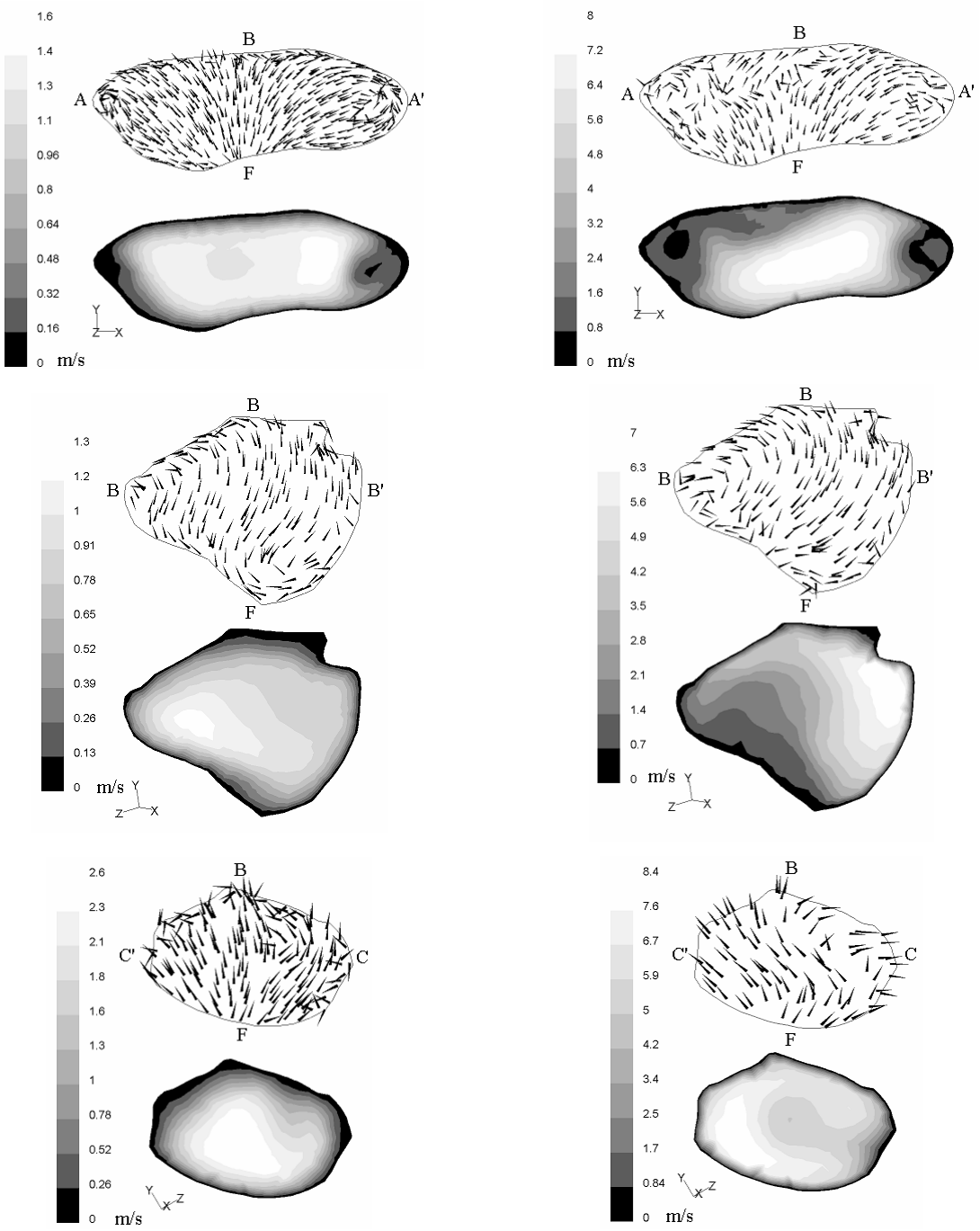

(a) (b)

Figure 5.4 – Secondary velocity vector and velocity contours plots at section A-A', B-B' and C-C' (Refer Fig. 5.3(c) for position of sections) for an inspiratory flow rate at (a) 15 l/min and (b) 60 l/min. The letters (B and F) on top and bottom of the vector graphs indicate where the Back and Front of the section are.

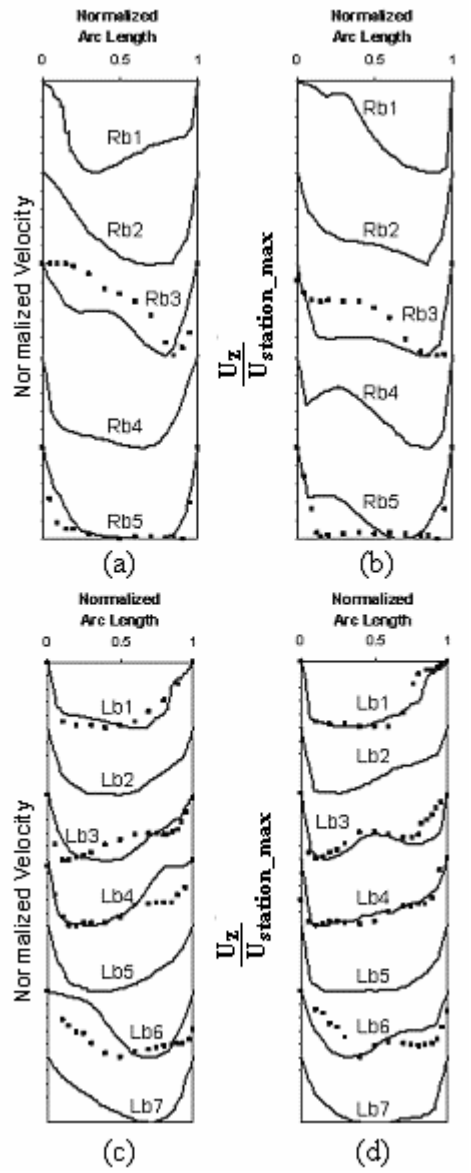

Figure 5.5 – Normalized velocity profile at bronchus for an inspiratory flow rate at (a) & (c) 15 l/min and (b) & (d) 60 l/min, plotted as a function of the normalized arc length. (Refer Fig. 5.3(c) for station position) The experimental data of Chang & El Masry (1982) are plotted as (■) for the corresponding stations.

Figure 5.5 depicts the common and the difference of velocity profile that both flow conditions (15 and 60 l/min) had. The velocity profiles in the right bronchus (Rb1) at the

lower flow rate was more moderate than higher flow rate and had a high peak near the lateral wall (abscissa 0) while the profile of the higher flow rate was highly skewed toward the inner wall of the bifurcation. The secondary profiles at section B-B' in Figure 5.4 correspond to the previous descriptions, but the velocity vector graph also indicates that the fluid at lower flow rate only tended to move toward the back of the airway due to the upstream vortex shading (cf. section A-A'). Whereas, the fluid motion at higher flow rate not only tended to move toward the back of the airway, it also moved toward the inner wall of the bifurcation (B').

Further downstream in the right upper (Rb2 and Rb3) and lower (Rb4 and Rb5) bronchi, the axial velocity profiles generally continued the basic structure from the previous profiles (Rb1). At lower flow rate, the profiles in the upper bronchi were skewed toward the inner wall of the second bifurcation while the velocity magnitudes were lower near the outer wall (abscissa 0). This phenomenon is likely to be caused by the flow separation or mild reverse flow near the bend of the first bifurcation (near Rb2) (Daily and Harleman, 1966). However, the higher flow rate was able to overcome the adverse pressure gradient near the outer wall of the first bifurcation due to its greater momentum (as discussed by Chang and El Masry (1982)). The velocity profiles in the lower bronchi at the lower flow rate were fairly blunt and almost symmetrical due to the small branching angle. On the other hand, due to the greater inertia forces (higher flow rate) from the upstream which caused significant pressure on the carina ridge of the second bifurcation, the velocity near the inner wall was either mild and reversed or very slow, so the velocity profiles were low in the inner wall and high in the outer wall of the second bifurcation.

Three sets of velocity profiles at left bronchus (Lb1 Lb2 and Lb3) are presented in Figure 5.5 . At the lower flow rate, profile at Lb1 was like a mirror image of the profile at the other side (Rb1) where the low velocity zone near the outer wall (abscissa 1) was caused by flow separation. But, the profiles at Lb2 and Lb3 show that the flow separation was reattached at a short distance from Lb1 due to the low velocity flow. With the higher flow rate, the profile at Lb1 had slow fluid motion near outer wall of the first bifurcation due to large branching angle where again the flow separation or mild reverse flow occurred near the outer wall of bifurcation. But the fluid at Lb2 and Lb3, near the outer wall (abscissa 1) soon accelerated

from a low velocity. This phenomenon can be explained by the transverse momentum exchange associated with higher Reynolds number flows as suggested by Chang and El Masry (1982). The secondary profiles at section C-C' in Figure 5.4 is virtually showing Lb3, but in a transverse plane, whereas the high velocity zone concentrated in the middle of the airway for the low flow rate condition. Here the fluid only tended to move toward the back of the airway due to the upstream vortex shading (cf. section A-A'). In contrast, the fluid motion at the higher flow rate was not only tended to move toward the back of the airway, but it also moved towards the inner wall (C').

At flow rate of 15 l/min, both the upper (Lb4 and Lb5) and the lower (Lb6 and Lb7) bronchi had peak velocities skewed toward the inner wall of the second bifurcation and a very low velocity near outer wall. This indicated flow separation. In comparison, there was no flow separation observed near the outer wall using the 60 l/min flow rate. Also the peak flow in the upper bronchi (Lb4) skewed toward the inner wall was relatively moderate compare to Lb4 at the 15 l/min flow rate. Surprisingly, the peak flow in the lower bronchi (Lb6) skewed more towards the outer wall of the second bifurcation, which is also the extension from the inner wall of the first bifurcation.

5.4.2 Regional Deposition Efficiencies

Deposition efficiency (DE) is an important quantitative parameter, defined as the percentage of particles that are trapped on a designated airway surface (such as bifurcation or zone) with respect to the total number of particles entering the respiratory system. As discussed in Model Validation, three bifurcations were divided as shown in Figure 5.1 (a). Figure 5.6 compares the deposition efficiencies at the first bifurcation (B1) and the second bifurcations at right bronchi (B2.1) and left bronchi (B2.2) and indicates how the flow rate affects the DE within different bifurcations. Figure 5.7 and Figure 5.8 summarize all the DE results collected within this numerical simulation and illustrate them with respect to individual bifurcation in three different inlet flow rates. Then, the DE results are not only made against particle diameter, but also against the mean Stokes number, as measured at the inlet, which is calculated by a number of variables (mean inlet velocity, particle diameter)

and constants (particle density, inlet diameter and air dynamic viscosity) (Refer Table 5.2 for Stokes number equation). Figure 5.7 (b), Figure 5.8 (b) and (d) reveal the DE characteristic in combination of fluid velocities (i.e. flow rates) and particle sizes.

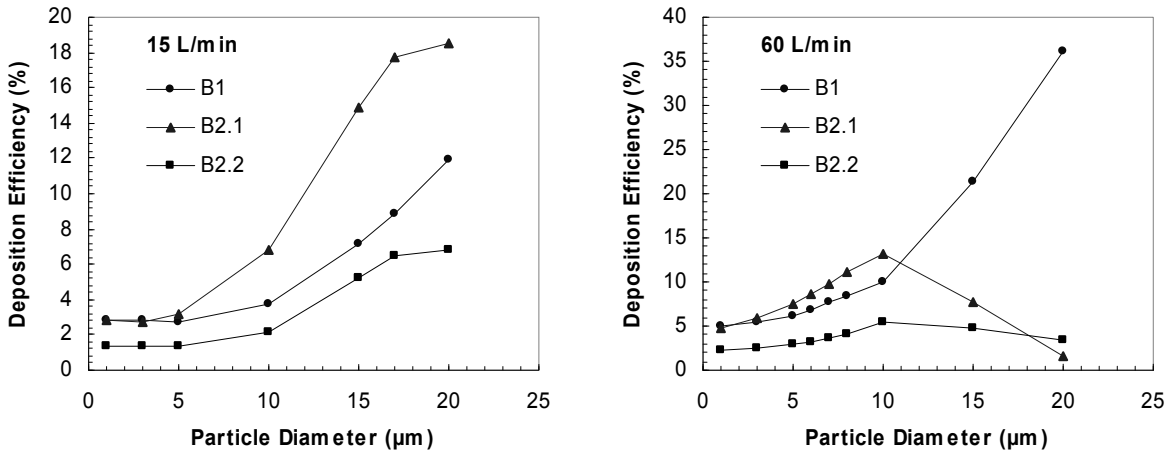

(a) (b)

Figure 5.6 - Plot of deposition efficiencies for two flow rates.

Figure 5.6 (a) shows that the DE at 15 l/min (inlet flow rate) in every bifurcation was quite even for particle sizes ranging from 1 to 5 micrometres and the DE in all bifurcations increased with the particle size. The DE at the right second bifurcation (B2.1) increased more considerably than both B1 and B2.2 as soon as particle size exceeded 5 micrometres. This was due to the fact that there was a peak velocity flow (cf. Figure 5.3 (a) – Profile T6) near the carina ridge in the right second bifurcation. Therefore, the peak velocity flow gave greater inertial force to the particles on the surroundings of the ridge and hence created higher particle deposition. As a result, the DE would increase further for larger particles due to the greater impact of the particles. Nevertheless, the second bifurcation in both sides (B2.1 and B2.2) seemed to reach their maximum DE in the tendency of the line when particle size reached 20 micrometres and on the contrary, the DE in the first bifurcation tended to increase further if the particle size were raised even more than 20 micrometres. Likewise, these

similar behaviours were also observed in Figure 5.6 (b) when the inlet flow rate was 60 l/min. There were differences in that the DE in the first bifurcation at 60 l/min inlet flow rate was higher than 15 l/min inlet flow rate for all particle sizes. This is due to the greater inertial force given by the larger flow rate. Also the DE in the second bifurcations reached the maximum DE with smaller particles (10μm) at 60 l/min compared to 15 l/min condition (20μm). Nonetheless, the DE in the right second bifurcation (B2.1) was still considerably higher than the left second bifurcation (B2.2). This was also shown by comparing Figure 5.7 (e) and (f) with a Stokes number smaller than 0.2. The reason that B2.1 had a higher DE than B2.2 was that the left bronchus (B2.2 side) is considerably longer than right bronchus. This means that particles have to travel further to reach the region of B2.2 which in turn reduces the chance for a particle to be trapped in region B2.2 because a part of the particles were trapped along the left bronchus (as shown in Figure 5.9 to Figure 5.12).

Figure 5.7 (a) shows that a higher flow rate gave a higher DE in the first bifurcation. This was more noticeable when the particle size increased. As expected, the high inertial force created by large particles and/or high flow rate led to a high DE. It should be noted that this only happened in the first bifurcation. In the second bifurcations, the previous characteristic only applied for certain ranges of small particles. As depicted in Figure 5.7 (c) and (d), the DE dropped when the particle size rose to a certain point. (e.g. at 60 l/min, DE dropped at 10μm in B2.1) This was due to the fact that more particles were already trapped in the first bifurcation as particle size increased (or flow rate increased) and it hence decreased the number of particles traveling to lower generations. As a result, the lower flow rate was more efficient to transport larger particles (e.g. 15 to 20μm) to the second bifurcation as shown in Figure 5.7 (c) and (d). On the other hand, a higher flow rate was better in transporting smaller particle (e.g. 1 to 10 μm) to lower bifurcations. Moreover, Figure 5.7 (b), (e) and (f) proved that mean Stokes number at the inlet is actually a good index of predicting DE. There are minor DE differences, however there are acceptable when the possible error (discussed in Model Validation) was taken into account.

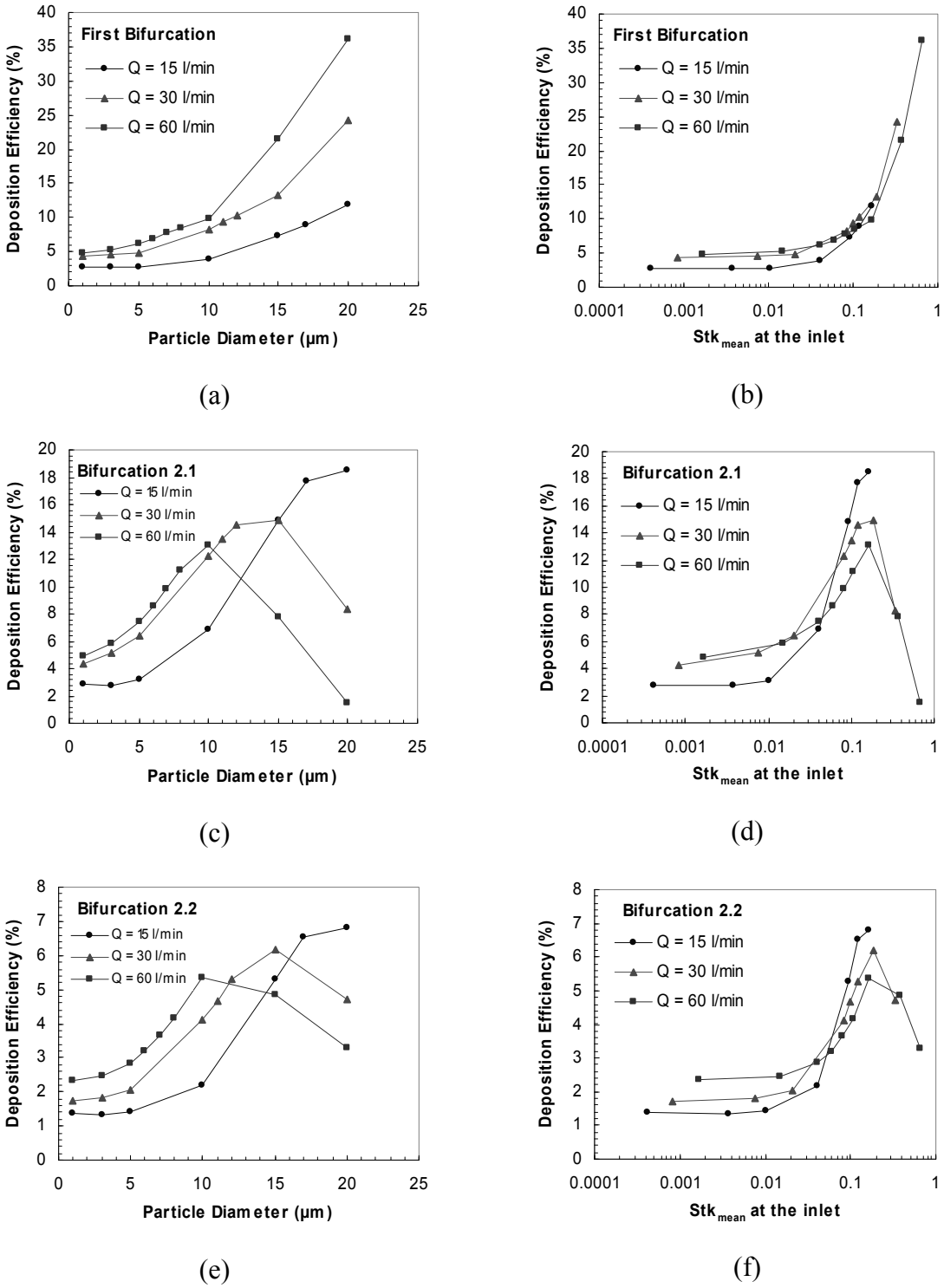

Figure 5.7 - Plot of deposition efficiencies for first bifurcation in the bifurcation airway model against particle diameter and mean Stokes number at the inlet.

5.4.3 Particle Deposition Pattern at Final Stage

Four graphical deposition patterns were illustrated on a three-dimensional airway model using four typical respiratory conditions (combination of two flow rates and two particle sizes) as shown in Figure 5.9 to Figure 5.12 . Although, the plot of DE against inlet mean Stokes number (St) already addressed the DE information in three typical locations (three bifurcations), the complete view of the deposition pattern can definitely help to investigate how the flow pattern affects the particle deposited into the airway in a more "viewable" term.

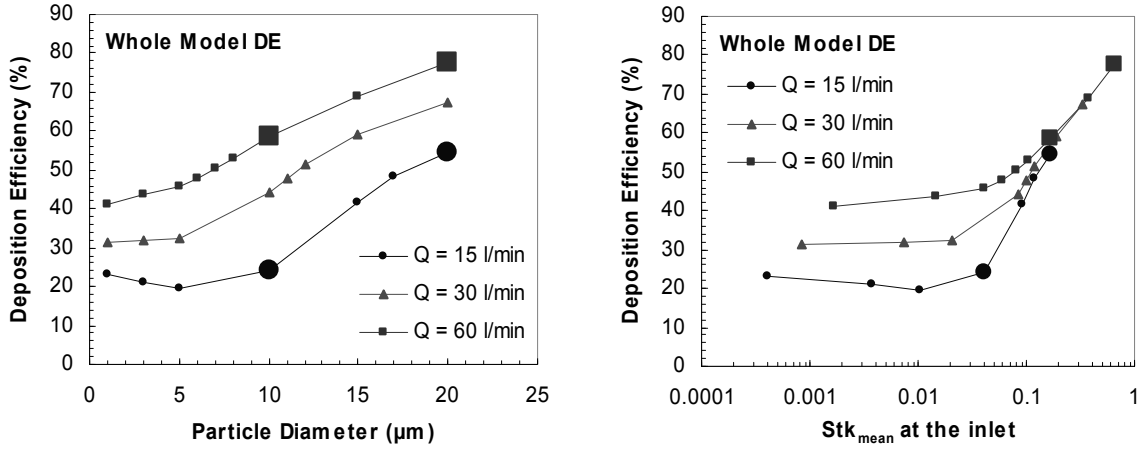

(a) (b)

Figure 5.8 - Plot of deposition efficiencies in the whole bifurcation airway model against (a) particle diameter and (b) mean Stokes number at the inlet. Enlarged points represent four selected conditions as shown in Figure 5.9 to Figure 5.12 .

Figure 5.8 illustrates the total percentage of particles deposited into the wall of the whole airway model. It shows that over the whole model the DE did not have the same characteristic as the DE in bifurcations in the plot of DE against St. Moreover, there was a large gap between the different flow rate's DE when St was less than 0.1. This is because the DE in the trachea and the first bifurcation dominated the DE in the whole model. Furthermore, DE in these two locations was especially sensitive to flow rate, rather than the particle size. Therefore, a high flow rate could directly increase DE in the trachea and the first bifurcation with no relation to Stokes number. This can be seen when two same Stokes

number conditions were compared (Figure 5.10 , DE = 55% @ St 0.166; Figure 5.11 , DE = 59% @ St 0.166). Both DE and St were almost the same, but the deposition patterns were markedly different, especially the pattern along the trachea.

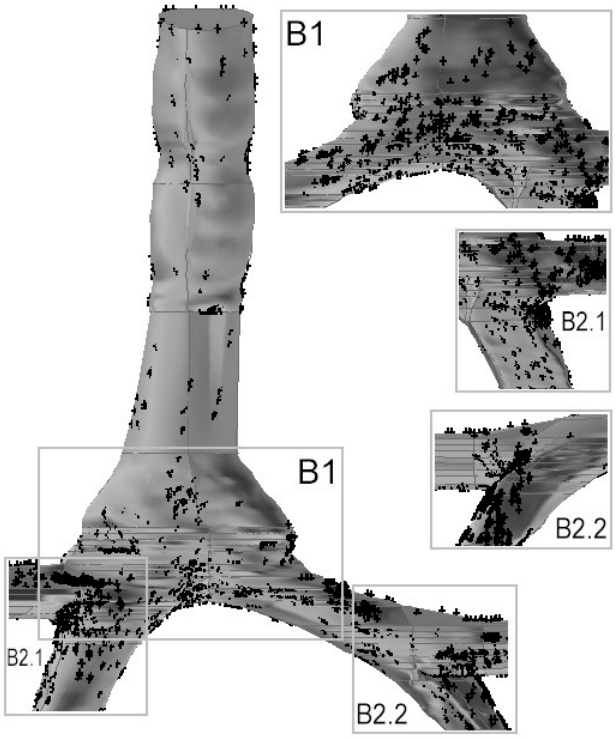

Figure 5.9 – Deposition pattern in front and back views for 15 l/min with particle diameter in 10 μm (St_{mean} = 0.042, Re_{mean} = 1447). Square windows are the back view of the bifurcations.

Figure 5.9 shows that the particles were diffused into every region quite evenly, although particle deposition was relatively concentrated in the bottom part of the airway due to air flow direction. Because of the low Stokes number, low DE in the whole model was expected as in Figure 5.8 . The axial velocity profile at station T6 in the trachea (Figure 5.3 (a)) for 15 l/min flow rate demonstrated that the "M" shape velocity profile gave relatively high particle densities in both sides (B2.1 & B2.2) and low densities in the middle (B1). Correspondingly, the velocity profile at station Rb1 (Figure 5.5 (a)) was moderate so that both the outside and the inside wall of second bifurcation (B2.1), as well as the carina ridge, collected noticeable

amount of particles. At another side, the velocity profile at station Lb3 skewed slightly toward the bottom bronchus, but still retained a moderate velocity in the middle. As a result, the bottom left bronchus and the carina ridge captured a higher amount of particles (see Box B2.2 in Figure 5.10). These phenomena were more obvious in Figure 5.10 where larger particles were injected with the same flow rate. The difference was that the locations mentioned contained higher particle densities and were less diffuse.

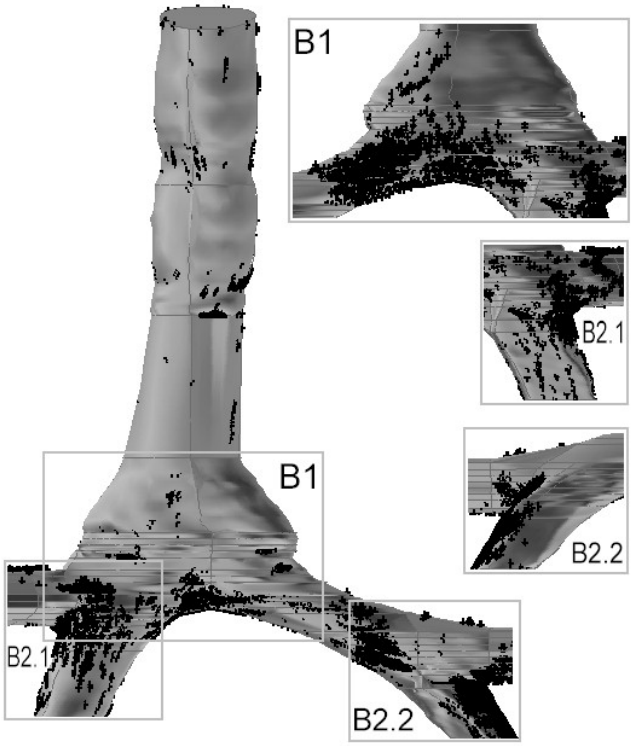

Figure 5.10 – Deposition pattern in front and back views for 15 l/min with particle diameter in 20 μm (St_{mean} = 0.166, Re_{mean} = 1447).

Figure 5.11 and Figure 5.12 show that a high flow rate increased the chance for the region facing directly towards the flow to collect a larger amount of particles. When smaller particles were injected (Figure 5.11), a diffusive phenomenon (not quite following the air flow direction) dominated the behaviour of particle transportation. This was why a large amount of particles deposited along the trachea. However, due to the moderate Stokes number, the model also contained high particle densities in all bifurcations and the inner wall

leading down from the carina ridge in all bifurcations. On the contrary, when large particle injected, convective phenomenon (particle follow the air flow direction) became dominated. In addition, particle densities were more intensive and concentrated into smaller areas in the cartilaginous rings along the trachea, the first bifurcation and the inner wall leading down from the carina ridge in the first bifurcation as shown in Figure 5.12 . The condition shown in Figure 5.12 seemed to capture fewer particles than in Figure 5.11 , but in fact, the total DE in the whole model in Figure 5.12 was much higher (≈ 20%) than Figure 5.11 as reflected in Figure 5.8 .

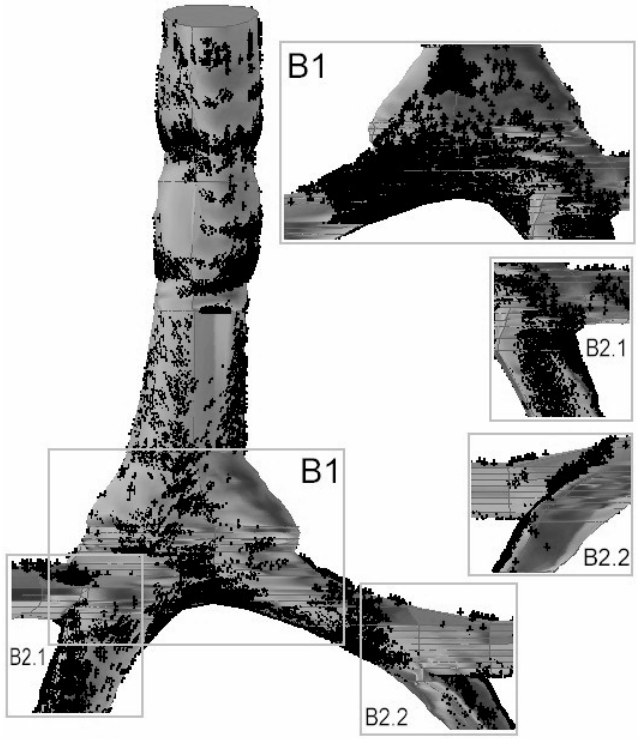

Figure 5.11 – Deposition pattern in front and back views for 60 l/min with particle diameter in 10 μm (St_{mean} = 0.166, Re_{mean} = 5789).

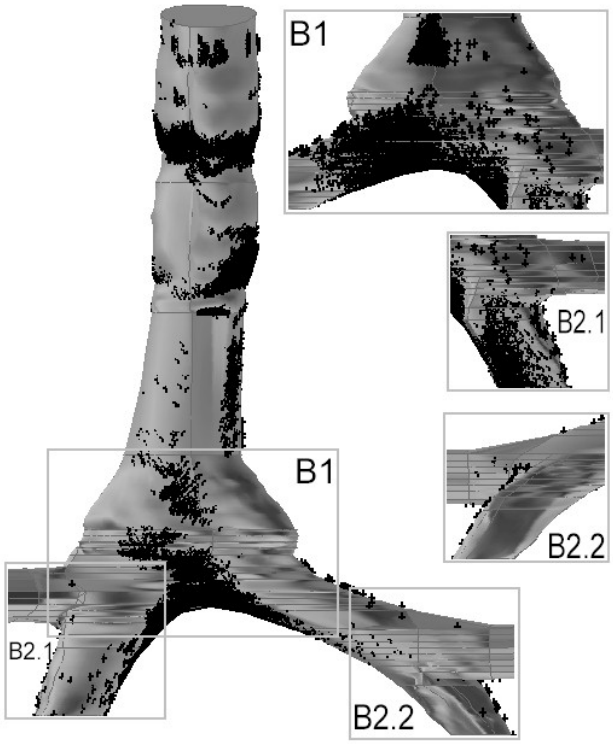

Figure 5.12 - Deposition pattern in front and back views for 60 l/min with particle diameter in 20 μm (St_{mean} = 0.665, Re_{mean} = 5789).

5.5 Chapter Summary

5.5.1 Summary of Outcomes

Velocity profiles, local deposition efficiencies (DE) and deposition patterns of aerosol particles in the first three generations (i.e. double bifurcations) of an airway model have been simulated numerically, in which the airway model was constructed from CT scan data of real human tracheobronchial airways. Three steady inhalation conditions, i.e., 15, 30 and 60 l/min, were simulated and a range of micron-particle sizes (1-20 μm diameters) were injected into the model. Results were then compared with experimental and other numerical results which had employed either similar model geometry or test conditions. The effects of inhalation conditions on velocity profiles and particle deposition were studied. The data

indicated that the local deposition efficiencies in the first bifurcation increased with a rise in the Stokes number (St) within St range from 0.0004 to 0.7. Within the same St range, DE in the second bifurcations (both left and right) was dropped dramatically after St increased to 0.17. Also, the second bifurcation in the right side (B2.1, closer to first bifurcation than left side, B2.2) was found to show a much higher (almost double) DE than the left side. This may be due to the fact that the left main bronchus is longer and has greater angulation than the right main bronchus.

Generally, the present simulation using a Computational Fluid Dynamic (CFD) technique obtained concurrent results with subtle differences compared to other works. Thus, it has proven that the current numerical methods would be suitable in interpolating into other airways model studies in which will be further discussed in the next chapter. However, due to omission of larynx in the model, which is known to significantly modify airflow and hence particle deposition, the present model may only serve as the "stepping-stone" to simulating and analyzing dose-response or inhalation risk assessment visually for clinical researchers.

5.5.2 Limitations of This Study

Several assumptions were made when carrying out this analysis and these has limited the present work to extrapolatable to real world scenarios. In terms of simulation, gravitational force is neglected and only constant particle entrance profile is studied. In anatomical and physiological terms, larynx and generations after third generations are excluded and thus, the larynx effect and effects of flow on upstream airways from additional downstream bifurcations are neglected. Only one constant inhalation is considered but in reality, tidal and cyclic breathing was proved to have great effect in particle deposition by Gurman et al. (1984).

Chapter 6
Study of Two Aerosol Delivery Methods

6.1 Introduction

After the evaluation of the CFD approach described in Chapter 5, it is then used to study the difference between two aerosol delivery methods routinely used clinically in terms of velocity profile, deposition efficiency and particle deposition pattern. The method of reconstructing the airway model from CT scans data used here is more superior than the method described in Chapter 5 and it is explained in this chapter. During the analysis process, advanced visualization technique is also developed. Therefore the potential "hot-spots" of high aerosol concentration can be immediately and easily observed. Results are validated with both experimental and theoretical data from other studies. Finally, some recommendations that could be useful to clinical researcher are drawn.

6.2 Methods

6.2.1 CT Scanning

Airway geometry was obtained through a computed tomography (CT) scan of the airways of a healthy 53 year old, non-smoking Caucasian female (164 cm height, 59 kg weight) for the first six generations (from trachea – G0 to bronchi – G5, hence Generation 0 to Generation 5). CT scan was performed using a CTI Whole Body Scanner (General Electric). The single-matrix scanner was used in helical mode with 1-mm collimation, a 40-cm field of view (FOV), 120 kV peak and 200 mA. At baseline, 2 cm axial length of lung caudad to the inferior pulmonary ligament was scanned during a single breath-hold, which yielded 146 contiguous images (slices in transverse direction, Z) of 1-mm thickness with voxel size 0.25* 0.25*1 mm.

6.2.2 Geometry Generation

The CT data was fed into an airway tree geometrical reconstruction software that can automatically identify the airway lumen in the CT image, (Pulmonary Workstation, VIDA Diagnostics, Iowa). The 3D model was then converted to IGES (Initial Graphics Exchange Specification) file using Geomagic Studio. Based on the IGES file, SolidWork 2005 was used to segment the model in terms of trachea, bifurcation and outlet. Finally, face, volume, mesh and extension tubes at outlets were created using GAMBIT 2.2.30 and a mesh file was produced, which was then read into FLUENT 6.2.16. A model was reconstructed as depicted in Figure 6.1 (a) using the given CT scans data of human tracheobronchial airways consisting of the first six generations from the trachea down to the fifth generation.

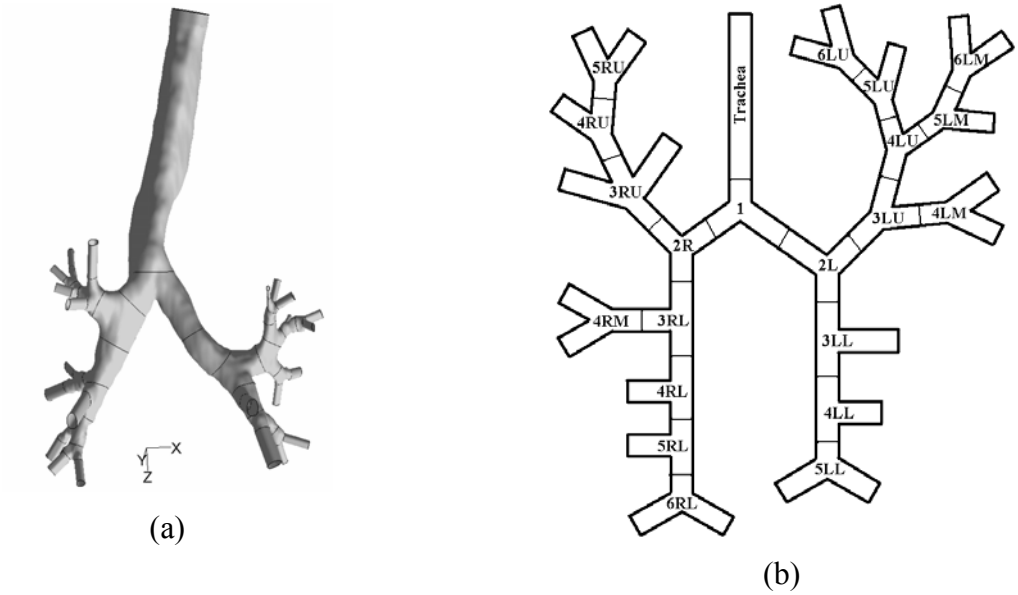

Figure 6.1 – Realistic six generations airway lung geometry (a) the front view of the studied 3D airway model with segmentation of bifurcation, the straight tube at the ends are not included in the study. (b) Schematic of the present respiratory airway model for branch identification in particle deposition analysis. Tags inside are the identification of each branch. The numbers in the front of the tags are arbitrarily assigned by generation number. Second letter represent the Left or Right sides of the lung. Letter, U, M and L at the end of the tag are upper, middle and lower respectively.

Extensions are added at the outlets of the airway model in order to avoid incompatibility between the outlet boundary conditions imposed numerically and the 3D flow effects

generated by the upstream airway geometry. Figure 6.1 (b) illustrated how the bifurcation region was segmented in the airways for measuring deposition efficiency (DE) and how the regions are tagged for identification in deposition efficiency analysis. The approximate geometric measurements of the model are provided in Table 6.1 . Figure 6.2 showed that the mesh size was gradually decreased when approaching smaller bronchi.

Table 6.1 – Airway model measurements

	Generation (Measurement in millimeters)											
	G0 (Trachea)		G1		G2		G3		G4		G5	
	CFD	Other	CFD	Other	CFD	Other	CFD	Other	CFD	Other	CFD	Other
Diameter	16	19	13-16	9-16	10-14	7-11	6-11	5-7	5-8	4-6	4-7	3-4
Length	105	110	15-46	21-60	11-32	13-22	6-14	9-16	7-13	8-14	7-12	7-12
Branching angle	N/A		29-48	12-78	17-90	12-78	18-54	12-78	33-54	12-78	11-35	12-78

Note. CFD, CFD model measurement; Other measurement is extracted from Weibel (1963) for diameter and length and Sauret et al. (2002) for branching angle. Weibel (1963) measured a cadaver's airway and reported in range value for each generation. Sauret el al. (2002)'s measured a health male volunteer's airway using CT images and reported the range value for all generations.

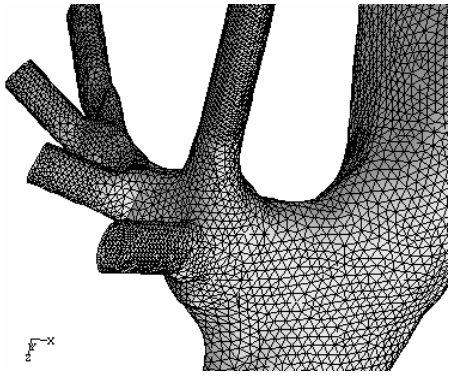

Figure 6.2 – Finite volume mesh of the six generations airway model

6.2.3 Simulation Conditions and Boundary Conditions

Two methods of aerosol medication delivery were simulated and the associated particle size tested was in the range of 3 to 10 micrometers in diameter. The input waveforms of flow rate at the inlet for both methods were shown in Figure 6.3 . The chosen particle size range is typical of those particles from inhalers that can reach the first few generations of airways (consisting of the trachea and the main bronchi (Edward, 2002)). These two methods are routinely used clinically to deliver aerosol medication through a metered dose inhaler and large volume spacer device. The Case 1 method (refer to Table 6.2 and Figure 6.3) requires patient inhale two liters in two seconds and then hold the breath for two seconds for aerosol to settle down, however the aerosol only entered in the first 700 ml (milliliters) of air through spacer device. On the contrary, the second method, Case 2 requires patient tidally breathe in and out for 5 breaths with a two seconds cycle with tidal volume of 400 ml; hence 10 seconds of breathing and total volume of air inhaled would be two liters as well. However, only one cycle of breath was simulated in this study for two reasons: one breath cycle was enough to achieve statistically independent results of deposition efficiency and hence deposition pattern would have been similar irrespective of how many breaths were numerical simulated; subsequently, it was found that one second of simulation time required 24 hours to run in a single CPU desktop, which was uneconomical. The major differences between Case 1 and 2 are not only the different flow rate and frequency, but also that there is no exhalation phase in Case 1. In contrast, Case 2 would have particle injection at the outlets during exhalation phase (for 1 second duration) in order to simulate unsettled particle in lower generations (> G5) re-entering the model after inhalation phase. The number of particle distribution at every outlet is assumed to be proportional to the area of outlet. Therefore, particles (aerosols) entered the model during the whole of both inhalation and exhalation phases. For simplicity, simple waveform expressed as sine function was used in both cases and applied at the inlet through User-Enhanced Function in FLUENT 6.2.16. The inlet velocity profiles were determined by running the fluid through a straight tube until it was fully-developed before the actual simulation took place. One cycle without releasing particle was also simulated to avoid start-up effects on the air-particle flow fields before the actual simulation took place.

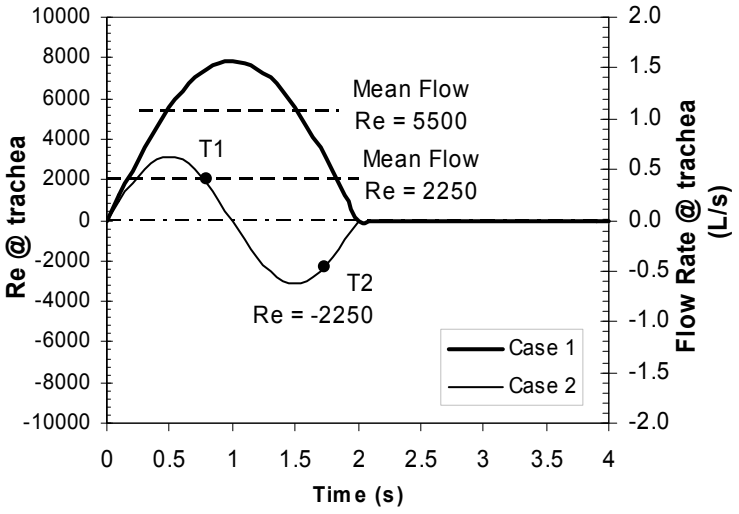

Figure 6.3 – The flow input waveforms used in this study

Table 6.2 – Representative respiration data and particle parameters

Method	Case 1	Case 2
Mean Respiratory rate (Q, L/min)	66	24
Mean Reynolds number[a] at inlet	5500	2250
Inspiratory capacity (ml)	2000	400
Time ratio of inspiratory phase (t_{in}/t_{total})	0.5	0.5
Frequency (cycle/min)	15	30
Peak inspiratory and expiratory Reynolds number at inlet	8649	3459
Particle diameter (d_p, μm)	5 & 10 (plus 3 & 7 for validation)	
Particle density (ρ_p, kg/m^3)	1550	
Mean Stokes number[b] at inlet for d_p = 5 & 10 μm	0.03861, 0.1544	0.01930, 0.07722

Note. U, D, ρ_{air}, μ, ρ_p and d_p are mean velocity evaluated as Q/A (A is the cross-sectional inlet area), inlet diameter, air density, air dynamic viscosity, particle density and particle diameter, respectively.

[a] Reynolds number, $\mathrm{Re} = UD\rho_{air}/\mu$

[b] Stokes number, $St = \rho_p d_p^2 U/(18\mu D)$

Particles were released at each time step (0.005 second) according to the preset particle flow rate which was assumed to be 300 micrograms per second (μg/s). A constant profile of particles was injected. The rationale for using constant entrance profile rather than parabolic profile is that the entrance profile is in fact unknown to what degree and skewed level of the profile should be after larynx effect at the inlet during inhalation phase and downstream effect at the outlets during exhalation phase. Zhang et al. (2005) already demonstrated that different flow rates and particle sizes would affect the particle deposition in the trachea after glottis and hence the particle profile would be distorted somehow due to distorted flow profiles, secondary flows and turbulent dispersion. For a simpler approach, a constant entrance profile of particle was chosen. The parameters of the respiratory and associated particle characteristics are summarized in Table 6.2 .

The airway wall was set as a trap in particle boundary condition for the same reason explained in Chapter 5. The flow distribution was calculated numerically in the present model where boundary condition of the outlets was set to pressure-outlet. It was suggested by FLUENT Inc. (2005) that if flow is not fully developed at the outlet or if there is back flow phenomena occurred (for example, during exhalation), pressure-outlet is recommended. The present numerical calculation showed that the flow distribution can closely match with other experimental and numerical studies as summarized in Table 6.3 .

Table 6.3 – Lobar air flow distribution (tracheal airflow percentages) in different human airway models

Lung	Right			Left	
Lobe	Upper	Middle	Lower	Upper	Lower
Present Model	21	8	29	13	29
Vial et al. - Subject A model (Vial et al. 2005)	15	7	33	21	24
Horsfield et al. (Katz and Martonen 1996)	21	9	25	20	25
Model used by Chang et al. (Corieri 1994)	20	10	25	20	25

6.2.4 Numerical Methods

The present numerical setting was similar to the first study (in Chapter 5), but the numerical solutions of the present simulation were solved using a later version of user-enhanced, commercial finite volume based program, FLUENT 6.2.16 (FLUENT Inc., 2005). The segregated method with implicit formulation was chosen to solve the unsteady-state governing equations by considering incompressible flows in the present simulation. The advantage of the fully implicit scheme was described in Chapter 5 already. The SIMPLEC algorithm with under-relaxation was selected for the pressure-velocity coupling.

The pressure interpolation scheme was set to be standard. The convective terms of the transport equations were all discretized using second-order-upwind scheme in order to obtain sufficiently accurate solutions. For stable and accurate iterative process, the relaxation factors for momentum and pressure were set to 0.5 and 0.2 respectively. In addition, the residual values of the governing equations and the transport equations (k-ω) were all set to converge at 10-3 with a small fixed time step size to be (Δt) 0.005 second for both simulation cases.

The particle trajectory equations were solved using the same stochastic tracking model and random-Eddy-lifetime (random walk) model in FLUENT 6.2.16 as FLUENT 6.1.22 while the effect of instantaneous turbulent velocity fluctuations on the particle trajectories for each time step was calculated after a converged flow fields was achieved. The drag parameter of the injected particles was again specified to be a smooth and spherical object.

The final number of particles was determined by increasing the number of particles inhaled (5μm was used) and increasing the particle injection time step until the deposition efficiency became statistically independent of the total number of particles. The DE is defined as the ratio of the number of particles deposited in a given region to the total number entering the region. The final number of particles was determined to be approximately 300,000 during inhalation and 500,000 during exhalation. Due to the low volume fraction (10-12%) of particles over fluid, one-way coupling between these two phases was assumed.

The mesh topology in this model was explained in Chapter 3. For this particular airway model, 500,000 elements were utilized. All calculations were performed on a Dell P4 3-GHz

PC workstation with 2 GB of RAM. A typical run time for fluid flow and particle transport simulations for Case 1 and Case 2 was approximately 96 hours and 48 hours respectively.

6.3 Model Validation

The deposition efficiency of particle in a six generations airway model for different particle sizes (i.e. Stokes number, Stk) in inhalation phase has been validated with various experimental data sets and theoretical models for the first three bifurcations for the sake of brevity. Three theoretical models were used to compare with the present numerical prediction. Cai and Yu (1988) developed a method to predict the particle deposition in an idealized, symmetrical bifurcation airway model. Only the interception and impaction mechanisms based on the interception distances and the stop of a particle in the cross section of the daughter tube were considered. An airway replica including the oral cavity, pharynx, larynx, trachea, and three generations of bronchi was developed by Cheng et al. (1999) and trend lines fitted on experimental data collected from the replica model with steady inhalation were presented. Balásházy et al. (1990) combined the action of inertia impaction and gravitational forces on a particle moving in three-dimensional circular bends. Subsequently, three experimental models were used for validation. Chan and Lippmann (1980) reported regional particle deposition efficiency in a human airway replica made from an adult cadaver for the first six generations starting from G0 trachea. Similar experiment was carried out by Zhou and Cheng (2005), but their model was limited to the first 4 generations. Kim and Fisher (1999) suggested modified logistic functions to describe DE vs. Stokes number for the first two bifurcations, which were based on the trend lines fitted on experimental data using double-bifurcating symmetrical glass tube models with steady inhalation. Finally, the present simulations for validation purpose used only constant inspiratory flow condition in order to correspond to other experimental and theoretical models. All collected data was plotted against the local Stokes number for the first three bifurcations and the local Stokes number is calculated by local velocity data.

Figure 6.4 (a) shows the comparison of present deposition efficiency in the first bifurcation with the data of two experimental models (Zhou and Cheng, 2005; Chan and Lippmann, 1980) and three theoretical models (Cai and Yu, 1988; Cheng et al., 1999; Balásházy et al., 1990). Zhou and Cheng's results basically showed agreement with the present results. Although, the slope of Chan and Lippmann's results had better agreement with theoretical models by Cai and Yu (1988) and Balásházy et al. (1990) than the present data and Zhou and Cheng's results, Zhang and Finlay (2005) already proved that cartilaginous rings affect DE significantly in the trachea and speculated that cartilaginous rings may be a critical element in influencing the prediction of particle deposition downstream. For that reason, although the present airway model was carefully replicated using the CT scan data, the resolution of the scan and the loss of details during file conversion process were major reasons for inaccurately reproducing the cartilaginous rings along the trachea. Therefore, the turbulence created by cartilaginous rings was not totally included in the present simulation in which may affect the prediction of deposition efficiency in the first few bifurcations.

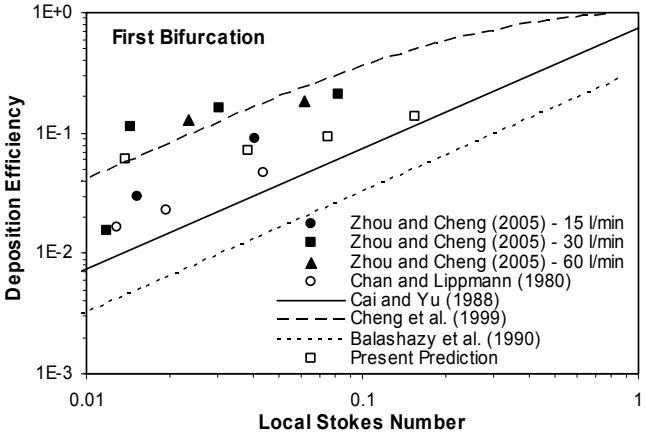

(a)

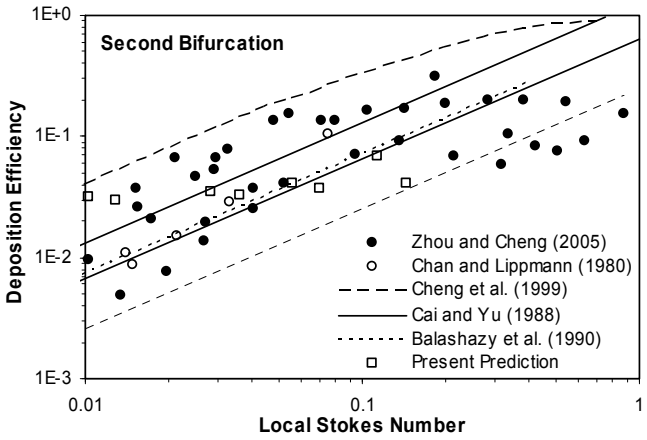

(b)

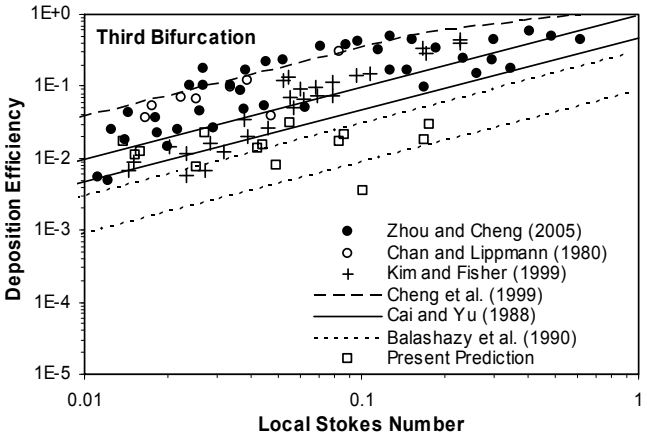

(c)

Figure 6.4 – Comparison of the deposition efficiency of the replica with reported lung cast deposition data, theoretical models and CFD predicted data at (a) the first bifurcation, (b) the second bifurcation and (c) the third bifurcation.

Figure 6.4 (b) and (c) showed the comparison of present deposition efficiency in the second and third bifurcation with the data of three experimental models (Zhou and Cheng, 2005; Chan and Lippmann, 1980, Kim and Fisher, 1999) and three theoretical models (Cai and Yu, 1988; Cheng et al., 1999; Balásházy et al., 1990). Similar comparisons as previously stated are found. The present results fall between two theoretical models (Cheng et al., 1999; Balásházy et al., 1990) and correspond well with Zhou and Cheng's results, that both results had shallower slope than Chan and Lippmann's data and theoretical data. However, the present results generally under predicted compared to all other models, except data from Balásházy et al. (1990). As Oldham (2006) pointed out that there are limited experimental data that can be used for comparison in validating CFD results, because even identical hollow cast model and the resulting digital model derived from CT scan would have discrepancies in either total deposition efficiency or local particle deposition pattern or both. When discrepancies and loss of details in model geometries (e.g. branching angle of bifurcation, bronchial length, etc.), the method of deposition measurements, the method of experiment and numerical setup are all critical issues in validating numerical results, thus the present study can only provide general comparison between two aerosol delivery methods, even the comparison between the present results and several experimental and theoretical models were drawn. However, the current developed model should be sufficient to present reasonably accurate information in terms of fluid-particle dynamics and particle deposition as well.

6.4 Results and Discussion

6.4.1 Axial Velocity and Secondary Velocity Profiles

The flow in a six generation airway model under two breathing conditions (i.e., Case 1 and Case 2) was simulated. For brevity, only the velocity profiles for Case 2, which include inhalation and exhalation phase, are displayed and discussed. Figure 6.5 (a) describes the station and section position in the present airway model for axial and secondary flow plot respectively. Axial velocity profiles at inspiratory and expiratory were plotted against with experimental data by Menon et al. (1984) for comparison. For easier comparison, axial velocity profiles were normalized, but magnitude of the axial velocity was still presented in Figure 6.6 and Figure 6.7 for a more detailed view of velocity magnitude distribution along the selected sections. Menon et al. (1984) measured oscillatory velocity profiles using a scaled human tracheobronchial airways model, which the geometry was closely comparable with the present numerical model. The numerical results generally had good agreement with the experimental results in terms of characteristic features. The small discrepancies in some of the stations were to be expected since the experimental model was made of smooth plastic tubes. Also, the flow rates and frequencies used in the experiment and in numerical simulation were different. The Reynolds number obtained in trachea was 2040 at 0.25 Hz in Menon et al. (1984)'s experiment compared to 2250 at 0.5 Hz in this numerical study.

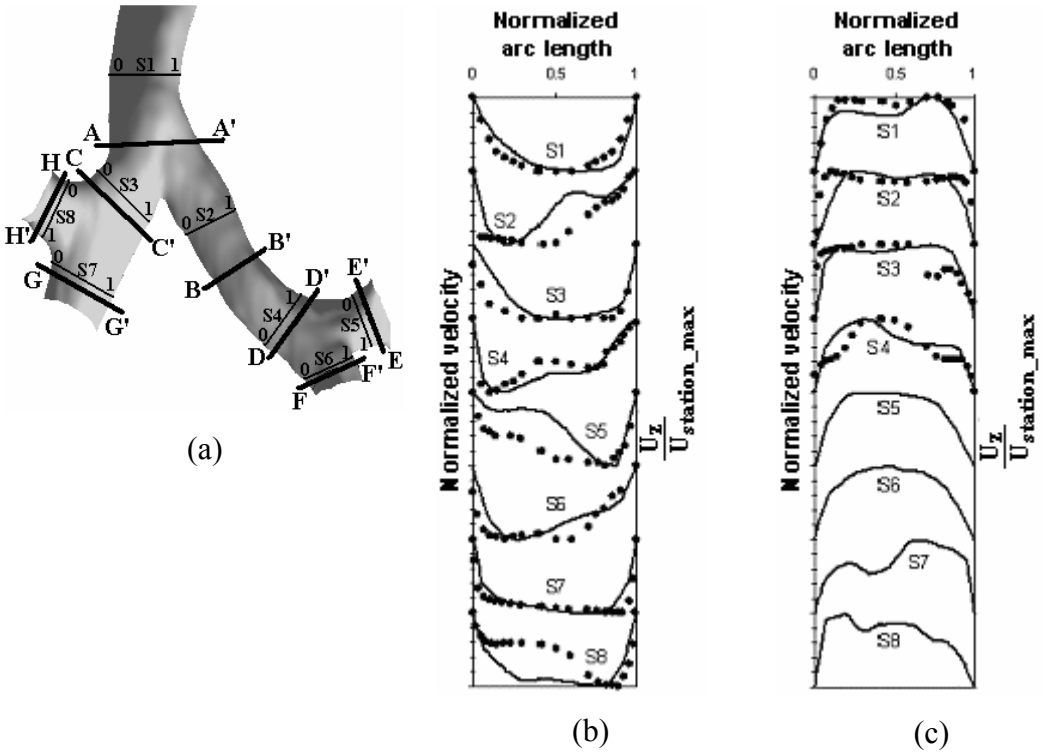

Figure 6.5 – (a) View of station and section position in the airway model for axial and secondary flow plot respectively. Letter, S represents station with thinner line. Abscissa 0 and 1 correspond to the marks, 0 and 1 in Figure 6.5 (a). Thicker line indicates the position of section that is taken to visualize the secondary flow in Figure 6.6 and Figure 6.7 . Normalized axial velocity profile for (b) inhalation at T1 and (c) exhalation at T2 for Case 2, plotted as a function of the normalized arc length. The experimental data of Menon et al. (1984) are plotted as (●) for the corresponding stations.

For inspiratory flow in Figure 6.5 (b), station 1 was a parabolic shape as expected from the fully developed flow, and then the flow split at the first bifurcation and profiles skewed toward the inner wall of the first bifurcation as shown in station 2 and 3. Profile at station 2 was more skewed than station 3 because right main bronchus was in a less branching angle than left main bronchus as depicted in Figure 6.5 (a). As flow started to redevelop in left main bronchus, station 4 became more moderate than station 2 as flow accelerated at the outer wall (Abscissa 1). Asymmetric velocity field continued to station 5 where axial profile was highly skewed toward inner wall of the second bifurcation due to the previous distorted

profile at station 4 plus the high branching angle. On the contrary, station 6 was much more moderate than station 5 because of the much smaller branching angle. In the right bronchi, flat shaped profile at station 7 was observed as similar reasons applied, small branching angle from the first bifurcation and less distorted velocity field from upstream(i.e., station 3). It was surprisingly found that station 8 was not as skew as station 5 when station 8 also had big branching angles as station 5. The rationale was that branching angle at station 5 was less than 90 degrees (approx. 60° from the center axis of left main bronchus), but station 8 has a branching angle of up to 90 degrees which may affect the flow, not in terms of a distorted profile, but in relation to a greater reduction of velocity magnitude. As an indication, axial velocity magnitude contour in Figure 6.6 indicates that right upper bronchi (section H) has greater rate of reduction by 1 m/s in maximum velocity than left upper bronchi (section E) by 0.5 m/s from their parent tubes (section C and D respectively).

Inhalation at T1

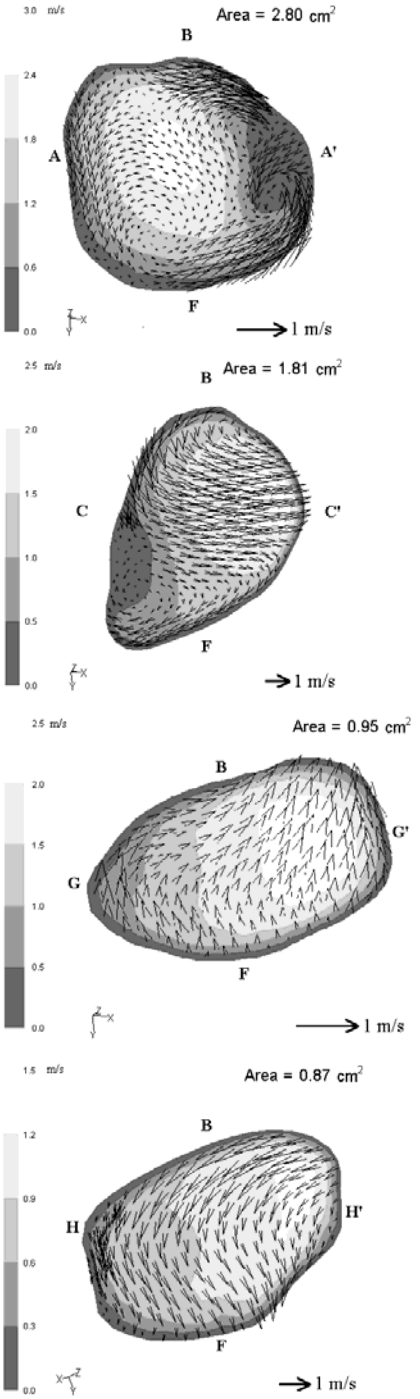

Exhalation at T2

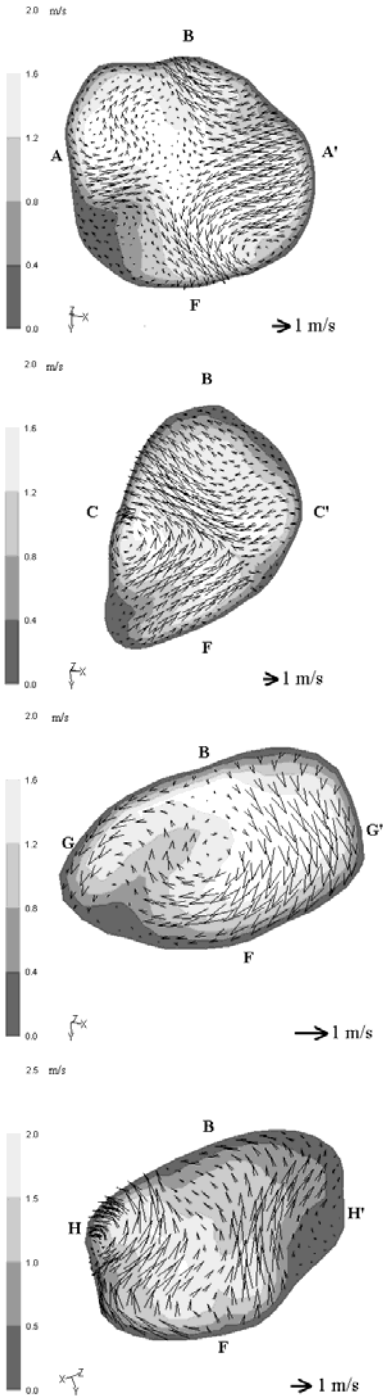

Figure 6.6 – Secondary velocity vector and axial velocity magnitude contour plots for inhalation at T1 and exhalation at T2 for Case 2 (Refer Fig. 6.5(a) for the position of section) The letters, B and F on top and bottom of the section indicate where the Back and Front of the airway are.

Inhalation at T1

Exhalation at T2

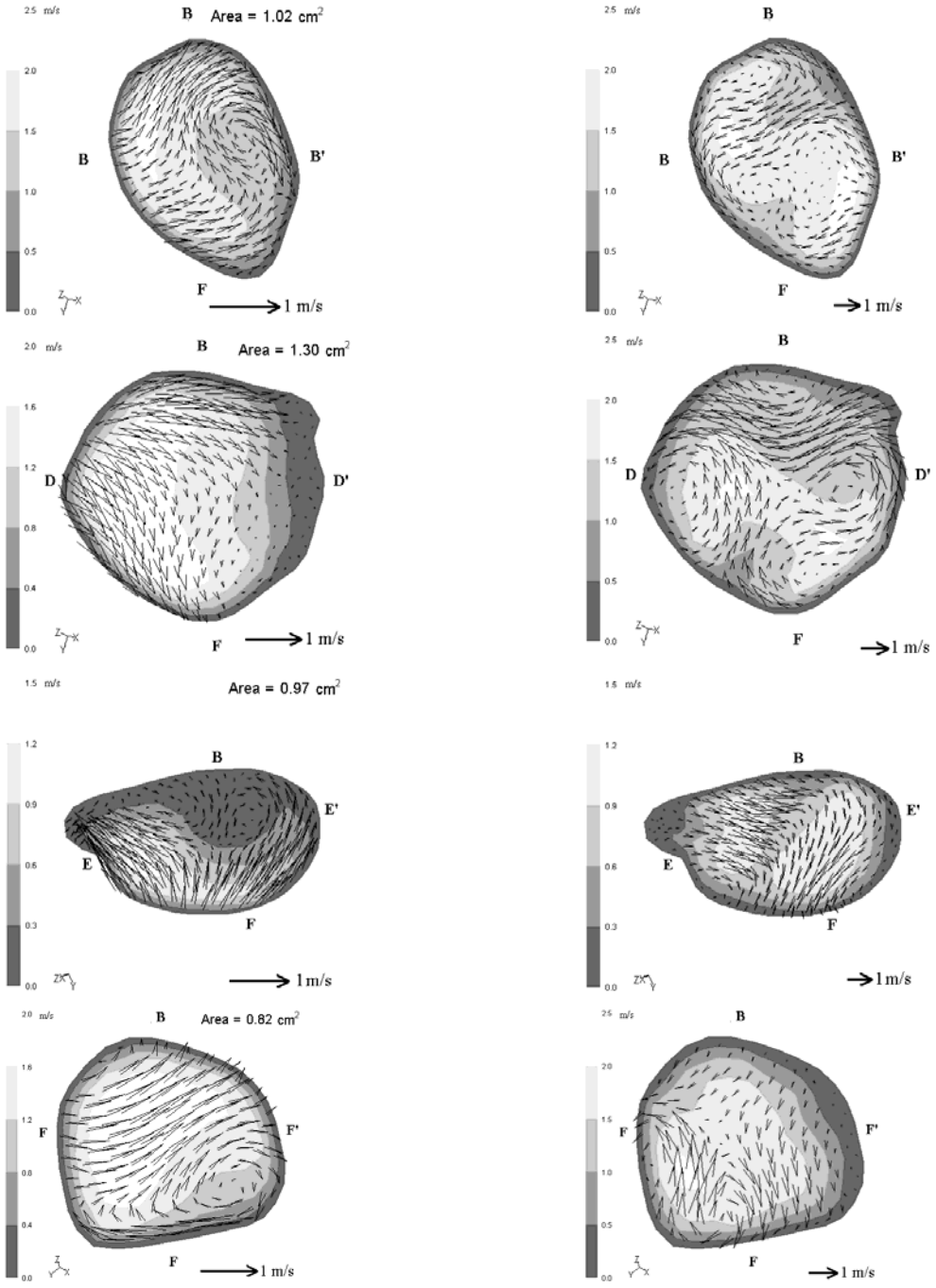

Figure 6.7 – Secondary velocity vector and axial velocity magnitude contour plots for inhalation at T1 and exhalation at T2 for Case 2 (Refer Fig. 6.5(a) for the position of sections) The letters, B and F on top and bottom of the section indicate where the Back and Front of the airway are.

In Figure 6.6 and Figure 6.7 , secondary motion vector with axial velocity contour on selected cross-sections described more details in flow phenomena. Secondary motions at the trachea (A-A') just before the flow reached the first bifurcation were interestingly found with several vortices generated which were not expected to be seen in straight trachea during inhalation. This was because a low pressure zone was created by the abnormal bend of the trachea above section A; the flow therefore pointed toward the left side of the airway (i.e., A'). When the flow reached the right main bronchus (section C), double vortices appeared as expected, as this phenomenon has been well documented by other researchers (e.g. Vial et al. 2005; Schroter and Sudlow, 1969; Zhang and Kleinstreuer, 2002). Then, axial velocity contours at section H had high velocity close to the inner wall of the second bifurcation, but high velocity zone was at outer wall at section G, which can be explained by the principle of preferential flow distribution for daughter branches with the smallest branching angle in which the principle was reported by Vial et al (2005). This was also why magnitude scale at section G was larger than section H and the same phenomenon was also detected in the left side (section E and F) in Figure 6.7 , hence magnitude at section F was larger than E. However, some discrepancies were observed as some re-circulations occurred at section E and F, but re-circulations at section E were relatively weaker which cannot affect too much in transportation of particles. On the other hand, section F had a stronger vortex close to the front side (F) in section F. In the left main bronchus, there were no double vortices observed in section B and D as explained in section C. The major rationale was because the abnormal bend in the trachea distorted the split of flow in the first bifurcation, and then the flow behaviour was completely different to section C which the flow pointed toward the first bifurcation's inner wall in the center. An obvious vortex occurred at section B and section D showed two strong motions traveling along the back of the section and pointing toward the front of the section.

Flow phenomena during expiratory phase were completely different for all the stations and sections. Instead of the air flow being split at each bifurcation, two or three (in trifurcation, tag - 3RU, the third right, upper trifurcation) air streams joined together from the daughter branches. As Zhang and Kleinstreuer (2002) reported, the axial velocity profile near flow

divider would have indentations at the centers. However, depended on the branching angle and the length and the cross-sectional shape of daughter branches, this phenomenon did not necessary happen at some stations. No indentations were observed at Station 3, 5 and 6 as shown in Figure 6.5 (c). There were several reasons that indentation phenomenon did not occur. Firstly, large branching angle such as at station 3, where upper daughter tube (station 8) was perpendicular to parent tube (station 3) whereas bottom tube (station 7) was almost collinear to its parent tube. It was obvious that no indentations would be expected. This was also confirmed at axial velocity contour in Figure 6.6 , section C. Since the realistic airway model contains nonplanar bifurcations, whereas the daughter tubes' plane is twisted compared to tubes either upstream or downstream, indentations therefore may be observed at the sectional axial velocity contour. Station 5 (section E) was one of these incidents. Axial velocity contour in Figure 6.7 , section E shows that "M-shaped" profile may be drawn if a plane was created from E to E'. Two high velocity zones were observed in which it meant that two airstreams were just joined together. On the other hand, another daughter tube (station 6, section F) did not have double high velocity zones due to unification of airstreams as shown in Figure 6.7 . Same reasons applied here as explained at station 3, where daughter tube was collinear to the parent tube (station 6). Other stations (i.e., station 1, 2, 4, 7 and 8) show either double or even triple peaks at their axial profiles. Triple peaks at station 8 were observed at trifurcation where three airstreams joined together.

Secondary motions during exhalation phase were turned and each daughter stream generated vortices. The result in parent tube was a sum up of number of vortices from its daughter tubes. Vortices were although not so apparent, it still roughly showed that number of vortices would gain up as airstreams proceeded to upstream. Section A indicated more vortices than its daughter tubes' section (section B and C). Likewise, sections at left main bronchus (i.e., section B and D) showed how secondary motions developed in a relatively long tube, where secondary motions revealed four strong vortices in which they were apparently the outcome of bulk streams. As it developed to upstream, same number of vortices can still be seen coarsely, but the intensity of vortices was much less as indicated by the length of vectors. As mentioned previously, branching angle and the length of daughter

tube can directly affect the indentations in axial velocity profile in parent tube; similarly, secondary motions were also influenced by the same factors. Therefore, it was not necessary to observe one or more vortices as air proceeded to upstream. This was showed in section C, E, F, G and H which only had two or less, or none obvious vortices showed. In terms of direction of secondary motions, motion vectors during expiration were generally directly opposite to motion vectors during inspiration.

6.4.2 Regional Deposition Efficiencies

Deposition efficiency (DE) is an important quantitative parameter, defined as the percentage of particles that are trapped on a designated airway surface (such as bifurcation or zone) with respect to the total number of particles entering the model. As mentioned, bifurcations were divided as shown in Figure 6.1 (b) with tag named individual bifurcation in order to locate their position in the airway model. Figure 6.8 and Figure 6.9 summarize all the DE results collected within Case 1 and Case 2 respectively (Refer Figure 6.3 and Table 6.2) and illustrate them with respect to individual bifurcation in two different conditions (i.e., cases) with two particle sizes.

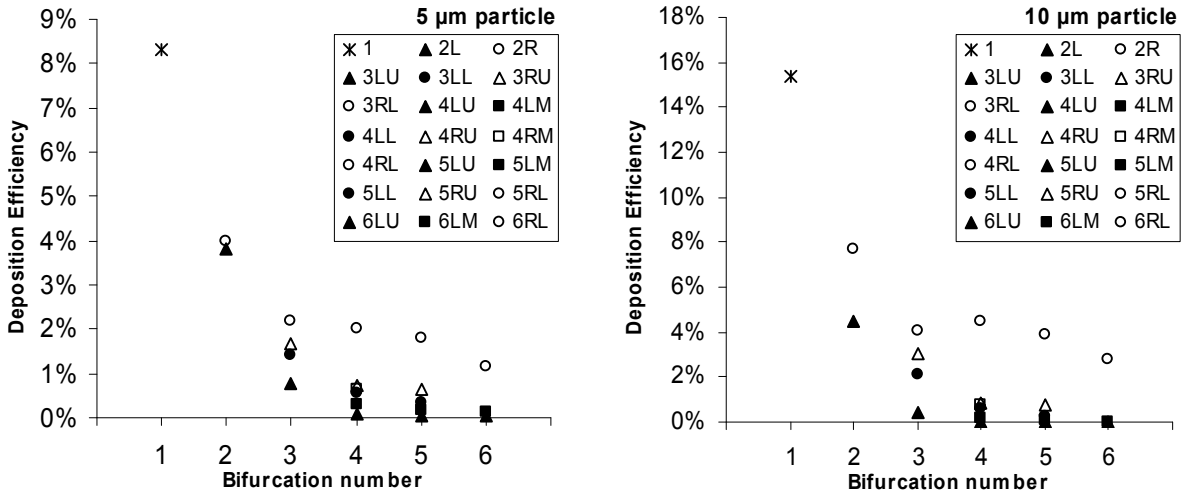

(a) (b)

Figure 6.8 – Deposition efficiency in each model's bifurcation (1 to 6) for particles of (a) 5 µm and (b) 10 µm computed for Case 1.

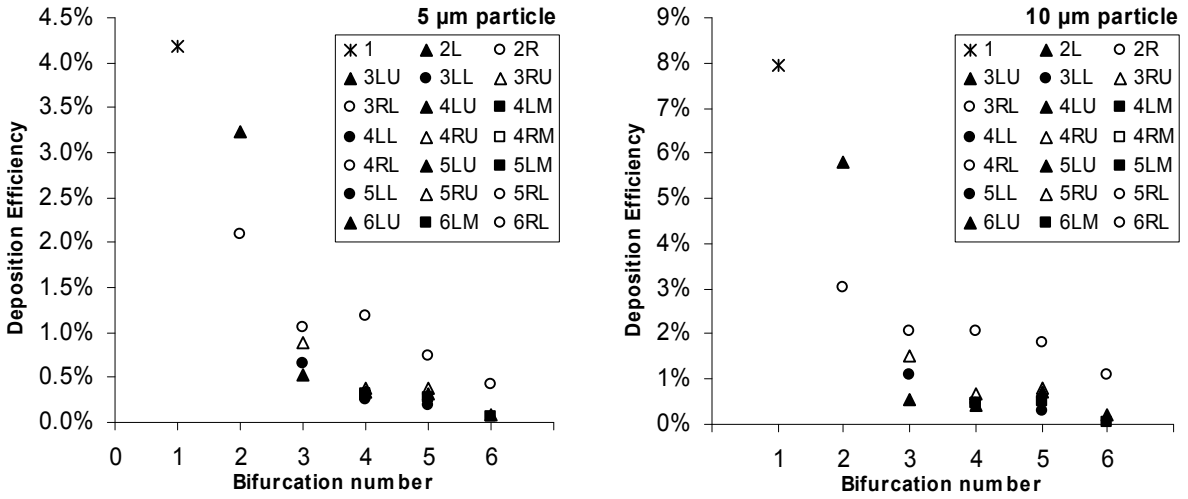

(a) (b)

Figure 6.9 – Deposition efficiency in each model's bifurcation (1 to 6) for particles of (a) 5 µm and (b) 10 µm computed for Case 2.

In two different aerosol delivery methods, higher flow rate at Case 1 was expected to lead to higher deposition efficiency than slower flow rate in Case 2 and all bifurcations in Case 1 were generally higher in DE than Case 2 in the same bifurcation. In addition, larger particle is a factor in higher DE. The DE differences within the same bifurcation number (i.e. same generation) were greater when particles were larger (e.g. In Figure 6.9 (a), DE difference in 2nd Bifurcations ≈ 1%; (b) ≈ 3%). These have well been proved by other similar studies (e.g. van Ertbruggen et al., 2005). Despite of second bifurcation, right side of the lung captured more particle than the left side in third, fourth, fifth and sixth bifurcations, but distribution among these bifurcations were quite even unlike first and second bifurcations. These phenomena might be due to the relatively large diameter branches in the right side which slowed the flow that leaded to relatively stronger secondary motion over its axial velocity, since secondary motion is the primary factor governing particle transport and deposition (Zhang and Kleinstreuer, 2002). Interestingly, second bifurcations in the right side captured more particles in higher flow rate (Case 1) but less particles were trapped in slower flow rate (Case 2) compared to second bifurcation in the left side. As mentioned in the last section,

based on the principle of preferential flow distribution for daughter branches with the smallest branching angle, deposition efficiencies at lower branches (i.e., tag with RL or LL) were generally higher than their upper bronchi (i.e., tag with RU or LU) at either left or right side of the lung as shown in Figure 6.8 and Figure 6.9 .

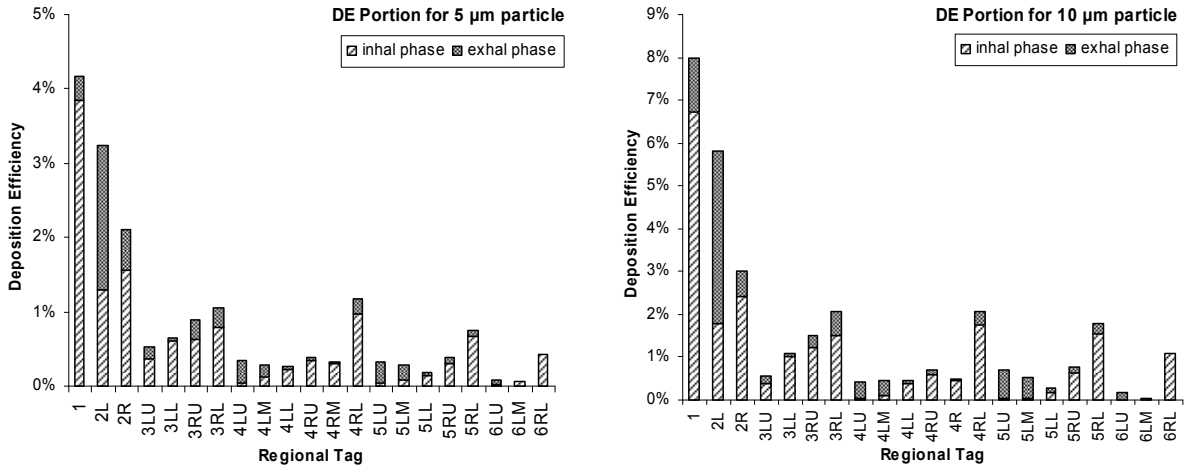

(a) (b)

Figure 6.10 – Deposition efficiency portion of particle trapped in the bifurcation during inhalation and exhalation phase for particles of (a) 5 µm and (b) 10 µm in Case 2.

The major difference between Case 1 and Case 2 was that Case 2 was complete cyclic flow at the inlet and Case 1 simulated inspiration only. Figure 6.10 is basically same as Figure 6.9 , but it also recorded the portion of deposition efficiency in inhalation and exhalation. One major finding was that deposition efficiency in exhalation can be vital in some of the bifurcations and same rule applied that larger particles caused higher DE during exhalation phase when comparing Figure 6.10 (a) and (b). DE during expiration in the first bifurcation contained certain portion (8% - 15%) of the final DE value. In second bifurcations, right sides can actually capture more particles as shown in Case 1 during inspiration, but as soon as expiration introduced, DE were surprisingly much higher in the left sides than right sides and large particles gave larger DE difference. In fact, secondary motions during exhalation at section C and D in Figure 6.6 and Figure 6.7 showed the primary differences that stronger secondary motions leaded by strong vortices in section D

directed higher particle deposition. In third bifurcations, bifurcation with tag 3LL was seemed to be less affected by expiration, but due to the limitation in reconstructing the airway, The bifurcation, 3LL contained one daughter branch and another one was outlet as shown in Figure 6.1 (b). Although trifurcation, 3RU also contained one daughter branch only, the other two outlets made up the DE prediction at expiration. Despite of 3LL, DE during exhalation took up around 20-30% portion in its final DE value. For brevity, the rest of the bifurcation also showed that DE at exhalation could play a critical role in particle deposition, although how much of a portion during expiration could not be justified using the data provided here because the missing of lower generations in the airway would definitely influence the deposition efficiency at certain level.

6.4.3 Particle Deposition Pattern at Final Stage

Four graphical deposition patterns were illustrated on a three-dimensional airway model using four typical respiratory conditions (combination of two cases and two particle sizes) as shown in Figure 6.11 to Figure 6.12 . There were several common findings for both cases in this particular model. The abnormal bend in the trachea just before the first bifurcation did not only affect the flow profiles as discussed previously, it also influenced the deposition pattern. This leaded to denser deposition pattern in the right side of the lung as shown in Figure 6.11 and Figure 6.12 . As expected, a wider spread of particles and denser concentration at the “hot-spot” were recorded for larger particle size, but the location for the particle deposition for both particle sizes were similar. The noticeable difference between Case 1 and Case 2 in respiratory condition was that influence on the deposition pattern by expiration was only included in Case 2. The deposition pattern that formed by both inspiration and expiration (i.e. Case 2) was discussed after the analysis of deposition pattern affected by inspiration only (i.e. Case 1).

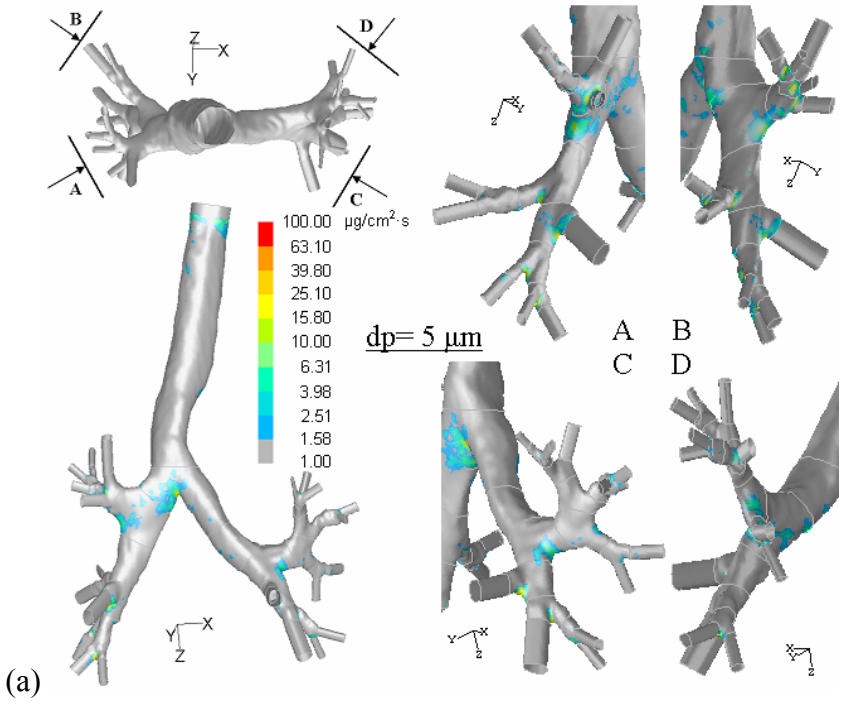

(a)

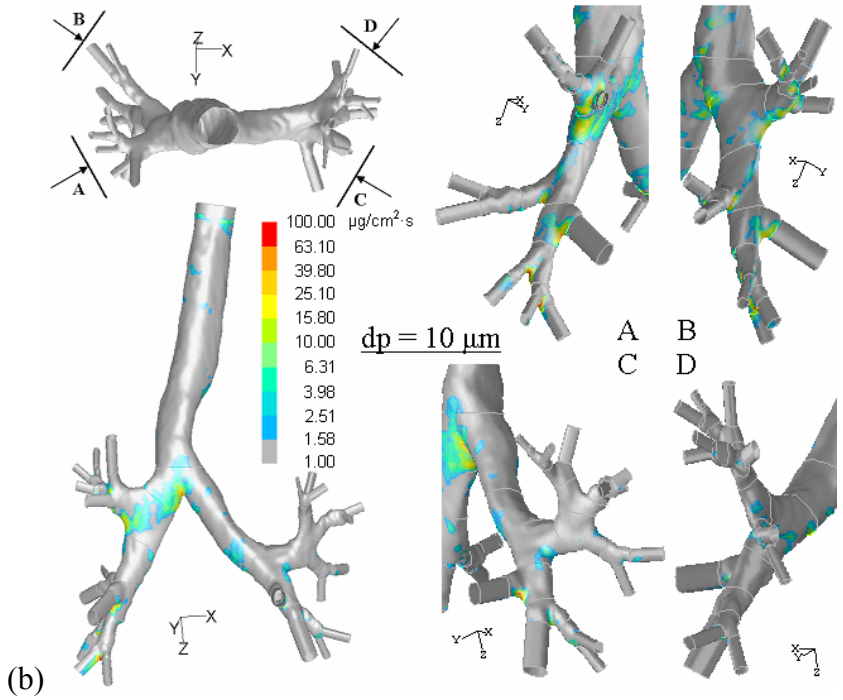

(b)

Figure 6.11 – Deposition pattern for Case 1 with particle size in (a) 5 µm ($St_{mean@inlet}$ = 0.03861, $Re_{mean@inlet}$ = 5500) and (b) 10 µm ($St_{mean@inlet}$ = 0.1544, $Re_{mean@inlet}$ = 5500). Four views in different angle of left and right bronchus. A and B are the enlarged views of right bronchus. Likewise, C and D are the enlarged views of left bronchus.

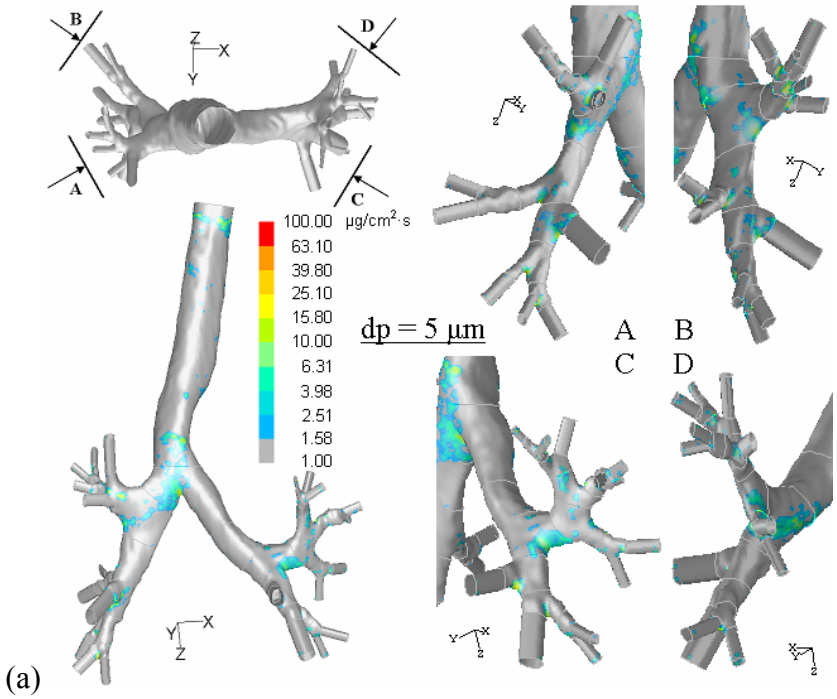

(a)

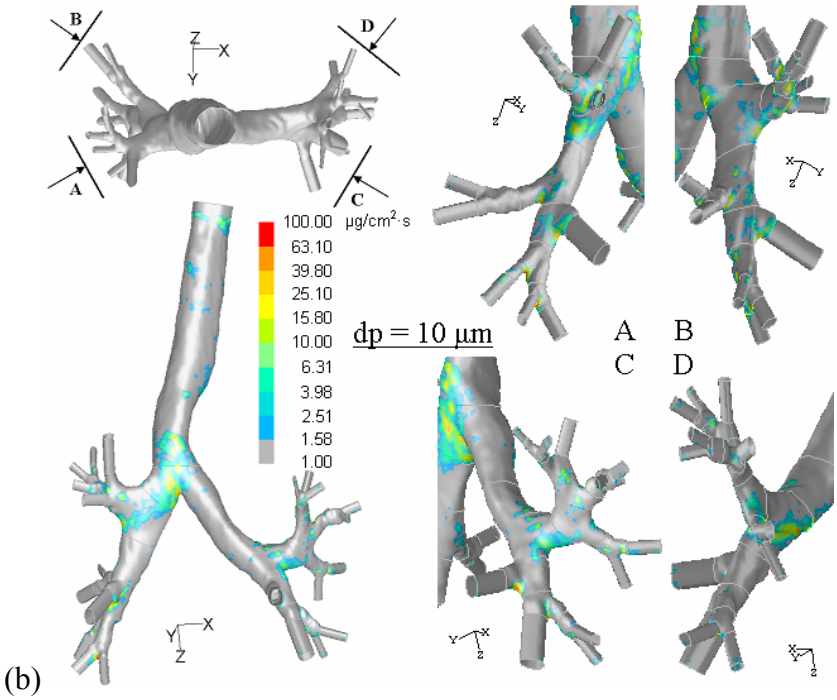

(b)

Figure 6.12 – Deposition pattern for Case 2 with particle size in (a) 5 μm ($St_{mean@inlet}$ = 0.01930, $Re_{mean@inlet}$ = 2250) and (b) 10 μm ($St_{mean@inlet}$ = 0.07722, $Re_{mean@inlet}$ = 2250). Four views in different angle of left and right bronchus. A and B are the enlarged views of right bronchus. Likewise, C and D are the enlarged views of left bronchus.

Deposition pattern during inspiratory phase was analyzed alone in Figure 6.11 , the formation of pattern can be roughly forecasted by analyzing through secondary motions during inhalation as shown in Figure 6.6 and Figure 6.7 . Due to the strong double vortices at section C (Figure 6.6 , Inhalation column), particles were concentrated at the inner wall of the first bifurcation during inhalation phase. On the contrary, particles were also transferred to the outer wall of the first bifurcation during exhalation, but due to the relatively weaker movement of flow, the concentration was not as dense and widespread as the inner wall. This phenomenon was obviously revealed when comparing views B in Figure 6.11 and Figure 6.12 . The secondary motions at section B (Figure 6.7 , Inhalation column) indicated an obvious, but relatively weak vortex compared to the axial velocity. The relatively small cross-sectional area of section B (1.02 cm^2 compared to section C, 1.81 cm^2) also suggested that the flow rate along that section of the tube was high which may push most of the particle downstream to section D. With the expansion in section D, secondary motions became relatively stronger to the axial velocity as shown in Figure 6.7 (inhalation column). Two strong motions indicated by the long vectors close to the back side of the airway (B) and the inner wall of second bifurcation (D) were observed. One was traveling along the back of the section from D to D'. Another one was pointing toward the front of the section from D to F in which both of these strong motions directed particles to the carina ridge and the back of the second bifurcation as shown in views C and D in Figure 6.12 respectively. A strong vortex close to the front side (F) of section F (Figure 6.7), helped to create one of the "hot-spots" in the carina ridge of the left, lower third bifurcation (i.e., tag - 3LL) as shown in the bottom of view C in Figure 6.12 .

Deposition pattern during exhalation phase was although not analyzed apart from inspiratory, the forming of pattern can still be forecasted by analyzing through secondary motions during exhalation as shown in Figure 6.6 and Figure 6.7 . Section C at exhalation (Figure 6.6 , exhalation column) explained why that was some depositions at the outer wall (C). It was caused by exhalation rather than inhalation since secondary motions during exhalation indicated that flow pointed to outer wall. Figure 6.10 already explained that exhalation added certain portion of total local deposition efficiency. In addition, a small re-

circulation was observed at the outer wall in which it may also transfer part of the particles away from the outer wall. By that reason, small deposition pattern appeared at the outer wall of the first bifurcation (Figure 6.12 , view B) in cyclic condition, Case 2, but no deposition in Case 1 was observed at the same location (Figure 6.11 , view B, outer wall of the first bifurcation). Most of the particle deposition during expiratory phase was not only concentrated along carina ridges in the bifurcation but extended upward. The difference can be seen at the first bifurcation between two respiratory conditions in Figure 6.11 and Figure 6.12 .

6.5 Chapter Summary

6.5.1 Summary of Outcomes

Velocity profiles, local deposition efficiencies (DE) and deposition patterns of aerosol particles in the first six generations of an airway model have been simulated using computational fluid dynamics, in which the airway model was reconstructed from computerized tomography (CT) data of real human tracheobronchial airways. The model is based on the airways of a middle aged, non-smoking, female patient with normal lung function. Two method of aerosol delivery methods (i.e. two respiratory and aerosols inhalation conditions) were simulated, as well as with different size of spherical aerosol particles (3-10 μm, 1.55 g/cm^3). Results were then compared with experimental and theoretical results which had employed either similar model geometry or test conditions. The effects of different delivery methods on particle deposition were studied. From a deposition efficiency perspective, an interestingly finding was that long breath hold following deep inspiration was not necessarily the better method in delivering aerosols to the lung periphery because the high fluid inertia (impaction) leading to a large percentage of aerosols being deposited in the first few airway generations. In certain conditions, slow complete cyclic breath with higher frequency can enhance the transportation of aerosol to the same location. These findings were supported by the regional deposition efficiencies in each bifurcation. Deposition patterns illustrated some of the potential “hot-spots” in the airways and showed

the differences between two delivery methods. Velocity profiles were also used to assist the analysis of deposition pattern forming. Some variations in all aspects between the present simulation and results from other investigators are also discussed.

6.5.2 Limitations of This Study

Several assumptions were made when carrying out this analysis which limited the degree to which the present work can be extrapolated to real world scenarios. In terms of simulation, only constant particle entrance profile at both inlet and outlet was studied. In anatomical and physiological terms, larynx and lower generations after the given model were excluded and thus, the larynx effect and effects of flow on upstream airways from additional downstream bifurcations were neglected. Input waveform was simplified in which may somehow affect the particle deposition efficiency and pattern, but in the best of author's knowledge, there is very little work on this matter, so the effect of input waveform in airway may be conducted in the future.

Chapter 7
Conclusions and Recommendations

7.1 Conclusion Remarks

7.1.1 Conclusions on Evaluation of CFD Approach for Flow-Particle Analysis

The validated CFD analysis of the realistic double bifurcation airway model proves that the present CFD model can provide reasonable results in terms of velocity profile, local particle deposition efficiency and particle deposition pattern. In the velocity profiles, the cartilaginous rings in the trachea would not cause major flow disturbances as indicated by the velocity profiles. This was demonstrated in Figure 5.3 with two different flow rates by comparing models with the rings (i.e., the present CFD model) and without them (i.e., Chang & El Masry's model (1982)). Comparing velocity profiles in the first and second generations (Figure 5.4) show that the velocity profiles generated with the CFD contained similar characteristics as Chang & El Masry's results (1982) in terms of general shape but with subtle velocity magnitudes due to different flow rates (i.e. Reynolds number) and model geometry.

The local deposition efficiency plots, using Stokes number as independent parameter, show that the CFD model can provide consistent prediction with only minor DE differences under various conditions. It was surprising to find that the DE's value in the first bifurcation was not necessarily higher than second bifurcation within certain range of Stokes number as this differed from the results obtained from the idealised model (c.f. Zhang et al., 2002 and Kim & Fisher, 1999). In fact, the DE's value in the second bifurcations can be the same, lower or higher than the DE in the first bifurcation, depending on the airway geometry and inlet Stokes number (i.e. flow rate and particle size). From the point of view of the deposition pattern, the cartilaginous rings in the trachea can have a major influence on DE in the

trachea. This is especially obvious when the flow rate is large. This has also been demonstrated by Zhang and Finlay (2005). Also, high particle densities were observed along carina ridge and the inner wall leading down from the carina ridge in all bifurcations, which is consistent with the numerical results of Zhang et al. (2002 a & b) and the experimental results of Schlesinger et al. (1982). However with various Stokes numbers, particle density can be concentrated in either (or both) inner wall.

Although, the local DE can be predicted by using Stokes number, conditions with same Stokes number are not necessarily the same in terms of local deposition pattern and particle density as demonstrated in Figure 5.10 and Figure 5.11 . Furthermore, since every person has a unique airway structure (especially for asthma patient with constricted airways), it is therefore important to evaluate the particle deposition pattern and particle density accordingly in order to provide accurate inhalation risk or dose–response assessment. This study demonstrated that CFD is capable of providing insight into fluid-particle dynamics and visualizing particle deposition for clinical assessment using the realistic human airway model reconstructed from CT scanned patient.

7.1.2 Conclusions on Two Aerosol Delivery Methods

The validated CFD analysis of the realistic airway model proved that the present CFD model can provide reasonable results in terms of velocity profile, local particle deposition efficiency and particle deposition pattern. In axial profile, indentations in the middle of the profile were confirmed, but it only occurred when both branching angles of daughter tube were appropriate. Daughter tube that is perpendicular to parent tube's axis will not create indentations. Axial velocity contour can assist to look at indentations at different angles. Secondary motions were important indication in predicting particles deposition pattern. Secondary motion vectors at inhalation and exhalation were generally directly opposite to each other. Also more vortices were observed during exhalation as reported by other researchers (e.g. Schroter and Sudlow, 1969; Zhang and Kleinstreuer, 2002). However, the number of vortices would not accumulate from downstream to upstream as proposed by previous studies. The rationale was that the branching angles of the daughter tubes were not

the same as the previous studies in which they were usually symmetrical or idealized. In deposition pattern perspective, the unique bend in the trachea directed particles to run into the right side of the lung. Some unexpected deposition locations were observed due to expiration, such as the outer wall of the bifurcation. Also, particle deposition efficiency can change dramatically in exhalation phase. These phenomena were more obvious in the first few bifurcations. As expected, deposition increased with particle size and flow rate. Therefore, a single deep inhalation and breathhold (Case 1 respiratory condition) had a higher deposition efficiency value than tidal breathing (Case 2) by around 15%-20% in total deposition efficiency (the entire model capturing particle rate). Based on these findings, if aerosols are to be delivered to the lung periphery (after the sixth generations), then tidal breathing will be the better delivery method. However, this finding requires further investigation. Aerosols are more likely to be transported to the lung periphery because fewer aerosols are to be captured in the upper airway, but lower generations may not be necessarily capture the remaining aerosols which may be directed back to the upper airway during expiratory.

Although, the local DE can be predicted by using Stokes number, conditions with close Stokes number value are not necessarily the same in terms of local deposition pattern and particle density as demonstrated in Figure 6.11 (b) and Figure 6.12 (a). Furthermore, since every person has a unique airway structure (especially for asthma patient with constricted airways), it is therefore important to evaluate the particle deposition pattern and particle density accordingly in order to provide accurate inhalation risk or dose–response assessment. This study demonstrated that CFD is capable of providing insight into fluid-particle dynamics and visualizing particle deposition for clinical assessment using the realistic human airway model reconstructed from CT scanned patient.

7.2 Clinical Significance of Results

There are several important points that can be concluded from this research that clinical investigators may find it useful:

- Stokes number although is a good indicator in providing regional deposition efficiency information, the local "hot-spots" still heavily rely on visualization of deposition pattern, especially the technique used in Chapter 6.
- Generally speaking, high flow rate and/or large particle size lead to high deposition efficiency in the first bifurcation and cartilaginous rings along the trachea.
- Bronchi in the right hand side usually capture more particles than bronchi in the left hand side.
- Particles often concentrate along the carinal ridges at the bifurcations and inner walls leading down from carinal ridges.
- In the aerosol delivery study, short inhalation and exhalation with small air volume (Case 2 in Chapter 6) gives lower deposition in the first six generations than long inhalation with large air volume. Therefore, if deposition into deeper locations of the lung is preferred, then slower breathing is required. On the contrary, if the treatment location is in the first few generations, then faster or moderate breathing is more ideal.
- Deposition efficiency and deposition pattern can be estimated roughly from the velocity profile along the airway.

7.3 Recommendations for Further Study

There are several improvements that can further enhance this study to extrapolate to real world scenario and understand the flow-particle phenomena more completely.

The first major issue is to include the upper airway consisting of the oral/nasal cavity down to larynx before joining the trachea and lower generations. It has been known that larynx effect can significantly influence the entering flow and particle profile at the trachea and hence it can affect the deposition considerably in the first few bifurcations within the airways. If more computer recourses (e.g. more powerful computer, enhanced software in imaging processing in reading CT scan, finer CT scans, etc) can be allocated, then lower generations (after generation 6) should also be included, because the entering profile at the outlets were assumed to be flat profile when cyclic flow case was applied at the current study. In fact, it has been known that flow profile after bifurcation is hardly a flat profile, the same applies to the particle entering profile during exhalation. The significance of this issue in the final outcome is hence not incorporated in this study.

Similarly, the input waveforms at the inlet in the study of aerosol delivery methods were not realistic when comparing to human breathing pattern. In addition, different breathing pattern should also be investigated. The following parameters can be varied in order to see what impact would occur on particle deposition, for example, frequency, flow rate and shape of waveform. In these aspects, further study should be conducted in the future. There has been little investigation of how much influence these can have on flow-particle interaction, if moisture and air temperature and temperature on airway's wall are applied in the simulation. In terms of the airway wall, it is known that there is no major influence on flow development if the movement of airway wall in the first few generations is included. This theory, however, may not apply to lower generations and hence the study of fluid-structure interaction within human airways should also be investigated.

The final recommendation is to obtain more CT scan data of other human airways for comparison and to quantify the results, providing a mature imaging processing technique is

developed. Some further studies that may interest the clinical investigator include airways before and after symptoms (such as asthma), operations (e.g. tissue tumor on the airway wall that obstructs the airway passage) and treatments (e.g., transporting aerosol drug into the lung using aerosol inhaler).

Appendix A

User-Defined Function at the inlet (used in Chapter 6)

```
/************************************************************************
  unsteady.c
  UDF for specifying a transient velocity profile boundary condition for Case 1
************************************************************************/
#include "udf.h"

DEFINE_PROFILE(unsteady_velocity, thread, position)
{
 face_t f;
 real t = CURRENT_TIME;

 begin_f_loop(f, thread)
   {
    F_PROFILE(f, thread, position) = 7.98011493782231*sin(0.5*3.14159265358979*t);
   }
 end_f_loop(f, thread)
}


/************************************************************************
  unsteady.c
  UDF for specifying a transient velocity profile boundary condition for Case 2
************************************************************************/
#include "udf.h"
DEFINE_PROFILE(unsteady_velocity, thread, position)
{
 face_t f;
 real t = CURRENT_TIME;


 begin_f_loop(f, thread)
   {
    F_PROFILE(f, thread, position) = 3.19204597512893*sin(3.14159265358979*t);
   }
 end_f_loop(f, thread)
}
```

References

Asgharian, B., and Price, O. T. 2006. Airflow distribution in the human lung and its influence on particle deposition. *Inhalation Toxicology*. 18:795-801.

Aykac, D., Hoffman, E. A., McLennan, G. and Reinhardt, J. M. 2003. Segmentation and analysis of the human airway tree from three-dimensional X-Ray CT Images. *IEEE Transactions on Medical Imaging.* 22:940-950.

Balásházy, I., and Hofmann, W. 1993. Particle deposition in airway bifurcations - I. Inspiratory flow. *Journal of Aerosol Science.* 24:745-772.

Balásházy, I., Hofmann, W., and Heistracher, T. 2003. Local particle deposition patterns may play a key role in the development of lung cancer. *Journal of Applied Physiology.* 94:1719-1725.

Balásházy, I., Hofmann, W. and Martonen, T. B. 1990. Inertial impaction and gravitational deposition of aerosols in curved tube and airway bifurcations. *Aerosol Science and Technology.* 13:308-321.

Bardina, J. E., Huang, P. G., and Coakley, T. J. 1997. *Turbulence modeling validation, testing and development.* Moffett Field, CA: National Aeronautics and Space Administration, Ames Research Center. (http://worldcatlibraries.org/wcpa/oclc/38071169)

Cai, F. S., and Yu, C. P. 1988. Inertial and interceptional deposition of spherical particles and fibres in a bifurcating airway. *Journal of Aerosol Science.* 19:679-688.

Calay, R. K., Kurujareon, J., and Holdo, A. E. 2002. Numerical simulation of respiratory flow patterns within human lung. *Respiration Physiology.* 130:201-221.

Cefalu, W. 2003, New Options in Exogenous Insulin Therapy, Diabetes Roundtable, viewed 22 May, 2006. <http://www.diabetesroundtable.com/courses/update/options.asp>

Chan, T. L., and Lippmann, M. 1980. Experimental measurements and empirical modeling of the regional deposition of inhaled particles in humans. *American Industrial Hygiene Association Journal.* 41:399-409.

Chang, H. K., and El Masry, O. A. 1982. A model study of flow dynamics in human central airways. Part I: Axial velocity profiles. *Respiration Physiology.* 49:75-95.

Cheng, Y. S., Zhou, Y., and Chen, B. T. 1999. Particle deposition in a cast of human oral airways. *Aerosol Science and Technology.* 31:286-300.

Clark, A. R. 1995. Medical aerosol inhaler: Past, present and future. *Aerosol Science and Technology.* 22:374-391.

Corieri, P. 1994. Experimental and numerical investigation of flows in bifurcations within lung airways. PhD Thesis. University of Libre de Bruxelles.

Comer, J. K., Kleinstreuer, C., and Zhang, Z. 2000a. Flow structures and particle deposition patterns in double-bifurcation airway models. Part 1. Air flow field. *Journal of Fluid Mechanics.* 435:25-54.

Comer, J. K., Kleinstreuer, C., and Zhang, Z. 2000b. Flow structures and particle deposition patterns in double-bifurcation airway models. Part 2. Aerosol transport and deposition. *Journal of Fluid Mechanics.* 435:55-80.

Crane, R. I., and Evans, R. L. 1977. Inertial deposition of particles in a bent pipe. *Journal of Aerosol Science*. 8:161-170.

Crowe, C. S., Sommerfeld, M., and Tsuji, Y. 1998. *Multiphase flows with droplets and particles*. New York, US: CRC Press.

Crowe, C. T., Troutt, T. R., and Chung, J. N. 1996. Numerical models for 2 phase turbulent flows. *Annual Review of Fluid Mechanics.* 28:11-43.

Daily, J. W., and Harleman, D. R. F. 1966. *Fluid Dynamics*. New York, US: Addison-Wesley.

Edwards, D. A. 2002. Delivery of Biological Agents by Aerosols. *AIChE Journal.* 48:2-6.

FLUENT Incorporated 2003. *FLUENT 6.1 Documentation*. Lebanon, NH FLUENT Incorporated. (NH: New Hampshire, US)

FLUENT Incorporated 2005. *FLUENT 6.2 Documentation*. Lebanon, NH FLUENT Incorporated.

Gurman, J. L., Lippmann, M., and Schlesinger, R. B. 1984. Particle deposition in replicate casts of the human upper tracheobronchial tree under constant and cyclic inspiratory flow. I. Experimental. *Aerosol Science and Technology.* 3:245-252.

Harrington, L., Prisk, G. K., and Darquenne, C. 2006. Importance of the bifurcation zone and branch orientation in simulated aerosol deposition in the alveolar zone of the human lung. *Journal of Aerosol Science.* 37:37-62.

Horsfield, K., and Cumming, G. 1968. Morphology of the bronchial tree in man. *Journal of Applied Physiology.* 24:373-383.

Horsfield, K., Gladys, D., Olson, D. E. Finlay, G. F., and Cumming, G. 1971. Models of the human bronchial tree. *Journal of Applied Physiology.* 31:207-217.

Katz, I. M., and Martonen, T. 1996. Three-dimensional fluid particle trajectories in the human larynx and trachea. *Journal of Aerosol Medicine-Deposition Clearance and Effects in the Lung.* 9:513-520.

Kim, C. S., and Fisher, D. M. 1999. Deposition characteristics of aerosol particles in sequentially bifurcating airway models. *Aerosol Science and Technology.* 31:198-220.

Kim C. S., Hu, S. C., Dewitt, P. and Gerrity, T. R. 1996. Assessment of regional deposition of inhaled particles in human lungs by serial bolus delivery method. *Journal of Applied Physiology.* 81:2203-2213.

Kreuzer, M., Muller, M. K., Brachner, A., Gerken, M., Grosche, B., Wiethege, T., and Wichmann, H. E. 2000. Histopathologic findings of lung carcinoma in German uranium miners. *Cancer* 89:2613-2621.

Li, A., and Ahmadi, G. 1992. Dispersion and deposition of spherical particles from point sources in a turbulent channel flow. *Aerosol Science and Technology.* 16:209-226.

Martonen, T. B. 1983. Measurement of particle dose distribution in a model of a human larynx and tracheobronchial tree. *Journal of Aerosol Science.* 14:11-22.

Menon, A. S., Weber, M. E. and Chang, H. K. 1984. Model study of flow dynamics in human central airways. Part III: Oscillatory velocity profiles. *Respiration Physiology.* 55:255-275.

Morsi, S. A., and Alexander, A. J. 1972. An investigation of particle trajectories in two-phase flow systems. *Journal of Fluid Mechanics.* 55:193-208.

Oldham, M. J. 2006. Challenges in validating CFD-derived inhaled aerosol deposition predictions. *Inhalation Toxicology.* 18:781-786.

Ounis, H., Ahmadi, G., and McLaughlin J. B. 1991. Brownian diffusion of sub-micrometer particles in the viscous sub-layer. *Journal of Colloid Interface Science.* 143:266-277.

Perzl, M. A., Schultz, H., Parezke, H. G., Englmeier, K. H., and Heyder, J. 1996. Reconstruction of the lung geometry for the simulation of aerosol transport. *Journal of Aerosol Medicine-Deposition Clearance and Effects in the Lung.* 9:409-418.

Pope, C. A., Dockery, D. W., and Schwartz, J. 1995. Review of epidemiological evidence of health effects of particulate air pollution. *Inhalation Toxicology.* 7:1-18.

Roland, N. J., Bhalla, R. K., and Earis, J. 2004. The local side effects of inhaled corticosteroids: Current understanding and review of the literature. *Chest* 126:213-219.

Sauret, V., Halson, P. M., Brown., I. W., Fleming, J. S., and Bailey, A. G. 2002. Study of the three-dimensional geometry of the central conducting airways in man using computed tomographic (CT) images. *Journal of Anatomy.* 200:123-134.

Schlesinger, R. B., Bohning, D. E., Chan, T. L., and Lippmann, M. 1977. Particle deposition in a hollow cast of the human tracheobronchial tree. *Journal of Aerosol Science*. 8:429-445.

Schlesinger, R. B., Gurman, J. L., and Lippmann, M. 1982. Particle deposition within bronchial airways: Comparisons using constant and cyclic inspiratory flows. *Annals of Occupational Hygiene.* 26:47-64.

Schorter, R. C., and Sudlow, M. F. 1969. Flow patterns in models of the human bronchial airways. Respiration Physiology. 7:341-355.

Shannon, J. M., and Deterding R. R. 1997. Epithelial-mesenchymal interactions in lung development. In: *Lung Growth and Development*. McDonald JA. New York: Dekker. p.81–118.

Su, W. C., and Cheng, Y. S. 2006. Fiber deposition pattern in two human respiratory tract replicas. *Inhalation Toxicology.* 18:749–760.

Van Ertbruggen, C. V., Hirsch, C., and Paiva, M. 2005. Anatomically based three-dimensional model of airways to simulate flow and particle transport using computational fluid dynamics. *Journal of Applied Physiology.* 98:970-980.

Varghese, S. S., and Frankel, S. H. 2003. Numerical modeling of pulsatile turbulent flow in stenotic vessels. *ASME Journal of Biomechanical Engineering.* 123:445-460.

Vial, L., Perchet, D., Fodil, R., Caillibotte, G., Fetita, C., Preteux, F., Beigelman-Aubry, C., Grenier, P., Thiriet, M., Isabey, D., and Sbirlea-Apiou, S. 2005. Airflow modeling of steady inspiration in two realistic proximal airway trees reconstructed from human thoracic tomodensitometric images. *Computer Methods in Biomechanics and Biomedical Engineering.* 8:267-277.

Weibel, E. R. 1963. *Morphometry of the human lung*. New York, US: Academic Press.

Wilcox, D. C. 1998. *Turbulence modeling for CFD*. La Cañada, California, US: DCW Industries, Inc.

Zhang, L., Asgharian, B., and Anjilvel, S. 1997. Inertial deposition of particles in the human upper airway bifurcations. *Aerosol Science and Technology.* 26:97-110.

Zhang, Y., and Finlay, W. H. 2005. Measurement of the effect of cartilaginous rings on particle deposition in a proximal lung bifurcation model. *Aerosol Science and Technology.* 39:394-399.

Zhang, Z., and Kleinstreuer, C. 2002. Transient airflow structures and particle transport in a sequentially branching lung airway model. *Physics of Fluids.* 14:862-880.

Zhang, Z., and Kleinstreuer, C. 2003a. Modeling of low Reynolds number turbulent flows in locally constricted conduits: A comparison study. *AIAA Journal.* 41:831-840.

Zhang, Z., Kleinstreuer, C., and Kim, C. S. 2002a. Gas-solid two-phase flow in a triple bifurcation lung airway model. *International Journal of Multiphase Flow.* 28:1021-1046.

Zhang, Z., Kleinstreuer, C., and Kim, C. S. 2002b. Cyclic micron-size particle inhalation and deposition in a triple bifurcation lung airway model. *Aerosol Science.* 33:257-281.

Zhang, Z., Kleinstreuer, C., Donohue, J. F., and Kim, C. S. 2005. Comparison of micro- and nano-size particle depositions in a human upper airway model. *Aerosol Science.* 36:211-233.

Zhao, Y., and Lieber, B. B. 1994. Steady inspiratory flow in a model symmetric bifurcation. *Journal of Biomechanical Engineering.* 116:488-496.

Zhou, Y., and Cheng, Y. S. 2005. Particle deposition in a cast of human tracheobronchial airways. *Aerosol Science and Technology.* 39:492-500.